IEEE Access
Multidisciplinary | Rapid Review | Open Access Journal

Received November 3, 2017, accepted December 24, 2017, date of publication January 4, 2018, date of current version February 28, 2018.

Digital Object Identifier 10.1109/ACCESS.2018.2789434

Variable Exponent Regularization Approach for Blur Kernel Estimation of Remote Sensing Image Blind Restoration

KUN GAO, ZHENYU ZHU, ZEYANG DOU, AND LU HAN
Key Laboratory of Photoelectronic Imaging Technology and System, Ministry of Education of China, Beijing Institute of Technology, Beijing 100081, China
Corresponding author: Kun Gao (gaokun@bit.edu.cn)

This work was supported in part by the Natural Science Foundation of Beijing, China under Grant 4152045, in part by the National Natural Science Foundation of China under Grant 60672082, and in part by the National High Technology Research and Development Program of China through 863 Program under Grant 2014AA7026082.

ABSTRACT Spatial remote sensing images are usually degraded during image capturing procedures mainly due to the mixed factors of atmospheric turbulence, spacecraft motion, and out of focus lenses. The real point spread function (PSF) of the whole imaging system is the convolution of all factors contributing to degradation. The exact degradation PSF model estimation is important for the image restoration result. In this paper, we considered the properties of the mixed degradation factors and proposed a new blind deconvolution model to simultaneously estimate and remove blurs from remote sensing images. Inconsistent with existing models, which mainly focus on only one degradation type and estimate blur kernel parameters using the fixed regularizer, we concentrated on the diversity of different PSF types and used the variable exponent regularizer to improve kernel flexibility. The proposed model could estimate not only single PSF types, such as motion, uniform, and Gaussian, but also composite PSFs of different types. Following the split Bregman method, we employed an efficient computational method, which did not require PSF initial values, to minimize the proposed cost function iteratively. Experimental results demonstrated the effectiveness and robustness of the proposed method for simulated and real remote sensing images with different PSFs' types.

INDEX TERMS Blind restoration, blur kernel estimation, variable exponent, alternating split Bregman.

I. INTRODUCTION

Generally, the blurring of satellite remote sensing images occurs for various reasons, such as atmospheric turbulence, spacecraft motion, out of focus lens, and other sensor properties [1], [2]. Blurriness can significantly degrade remote sensing image quality, which lowers the performance of various remote sensing applications, such as object detection, tracking, and disaster monitoring. Although image quality can be improved using complex optical systems, such as free surface design [3], [4], the costs are excessive. Therefore, a method for deblurring the degraded image is actively required for several remote sensing applications. One common mathematical model for the forward blur process may be expressed as

$$u(x, y) = k(x, y) \otimes f(x, y) + n(x, y) \tag{1}$$

where $u(x, y)$, $f(x, y)$, $k(x, y)$, and $n(x, y)$ are the blurred image, unknown sharp image, point spread function (PSF), and additive noise, respectively; and $\otimes$ represents the convolution operator. If $k(x, y)$ is known, the model becomes a non-blind deconvolution problem, which provides very good results. However, the PSF is difficult to obtain in practice, and the task of blind deconvolution is to simultaneously estimate $f(x, y)$ and $k(x, y)$ given only the degraded image, $u(x, y)$.

In the general image processing field, many methods have been proposed to address blind deconvolution [5]–[7], such as spectral and cepstral zero estimation [8]–[10], statistical estimation [11]–[13], wiener filtering [14]–[16], learning based [17]–[19], energy based [20], [21], etc. For remote sensing images, researchers have often estimated the PSF using specific features or objects (point source, edges, etc.). Commonly used approaches include the knife edge [22], sparsity based regularization [23], and pulse methods [24].

Since blind image deconvolution is a highly ill-posed problem, regularizers must be added to make the problem well-posed. A recent trend in blind image deconvolution

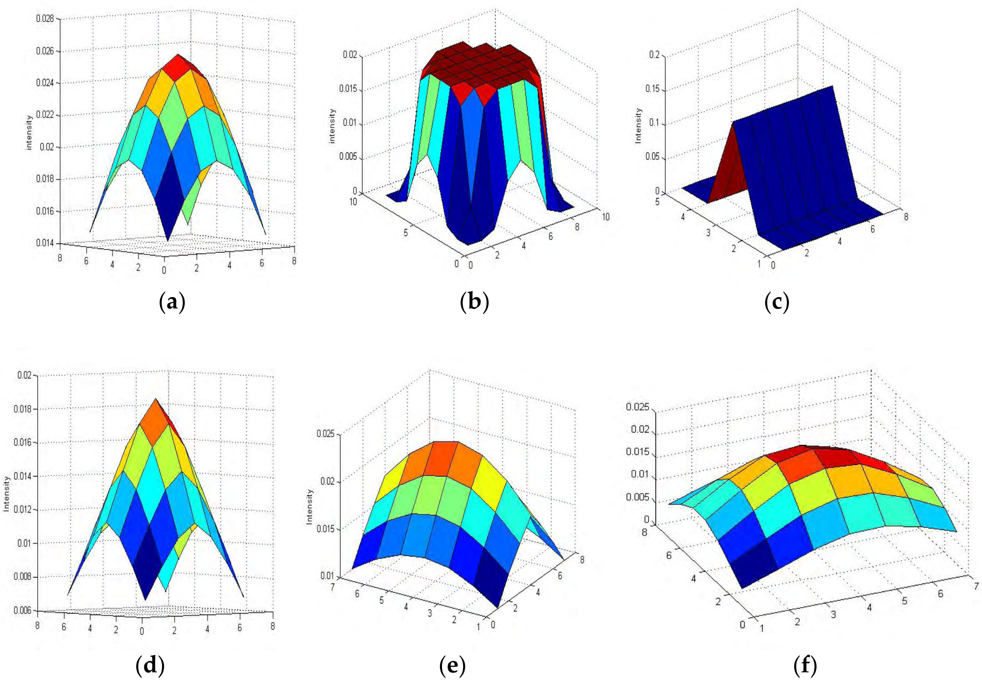

FIGURE 1. **Different point spread function (PSF) compositions: (a) Gaussian; (b) Disk; (c) Motion; (d) Gaussian-disk; (e) Gaussian-motion; and (f) Gaussian-disk-motion.**

focuses on extending regularization theory to address image deconvolution. Chen *et al.* [25] proposed a soft double regularization approach to parametric blind image deconvolution that could estimate many well-known parametric PSFs, such as motion, uniform and Gaussian blurs. Kenig [17] employed example based machine learning techniques for modeling the space of point spread functions. Tzikas *et al.* [11] proposed a sparse kernel based model for the PSF using priors based on the Student's t probability density function. The performance of their method was superior to Gaussian priors and total variation (TV) [30] based methods. Keuper *et al.* [26] proposed a regularization method deconvolution kernel on widefield data based on imposing constraints on the PSF in the frequency domain, which is easy to describe and is well localized. Krishnan *et al.* [27] introduced a new type of image regularization that produced the lowest cost for a true sharp image. You and Kaveh [28] used the Tikhonov regularizing term to capture the PSF smooth properties. Chan and Wong [29] proposed a TV regularization based approach to effectively restore piecewise constant PSF. Liao and Ng [31] used a second order difference regularization term to recover PSF. A recent study in Reference [32] used the Huber-Markov random field prior to model both remote sensing images and PSF. Bayesian methods are also frequently used in blind restoration. Such methods use auto regressive (AR) and moving average (MA) to model the image and PSF. Under this framework, the objective of blind deconvolution is to estimate image and blur kernels using statistical tools such as the expectation maximization (EM) [33], maximum likelihood (ML) [34], or

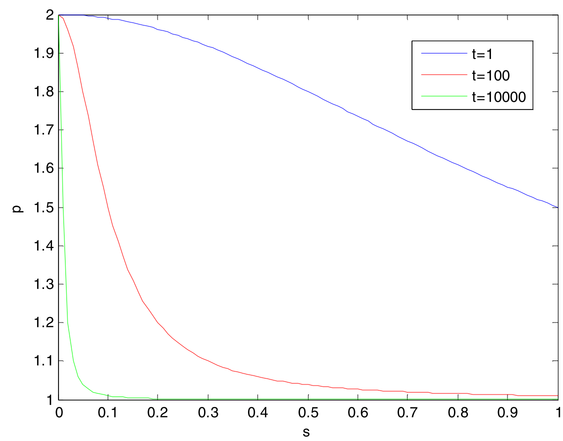

FIGURE 2. **Regularization parameter *p* for different parameter values.**

generalized cross validation (GCV) [35]. However, the smoothness constraint of the image and PSF, which is equivalent to regularization methods, is implicitly incorporated into these algorithms via the space invariant AR model [35]. Thus, these techniques are not appropriate for blocky images and sharp kernels. Babacan *et al.* [36] incorporated a TV function as the image priori and an AR model as the blur priori.

For remote sensing applications, PSFs have some fixed degree of parametric structure. If we only consider atmospheric turbulence as the cause of degradation to the image, the PSF would be Gaussian, which is smooth and non-sparse. If an out of focus lens is the main reason, then the PSF would be piecewise constant, which has sharp edges.

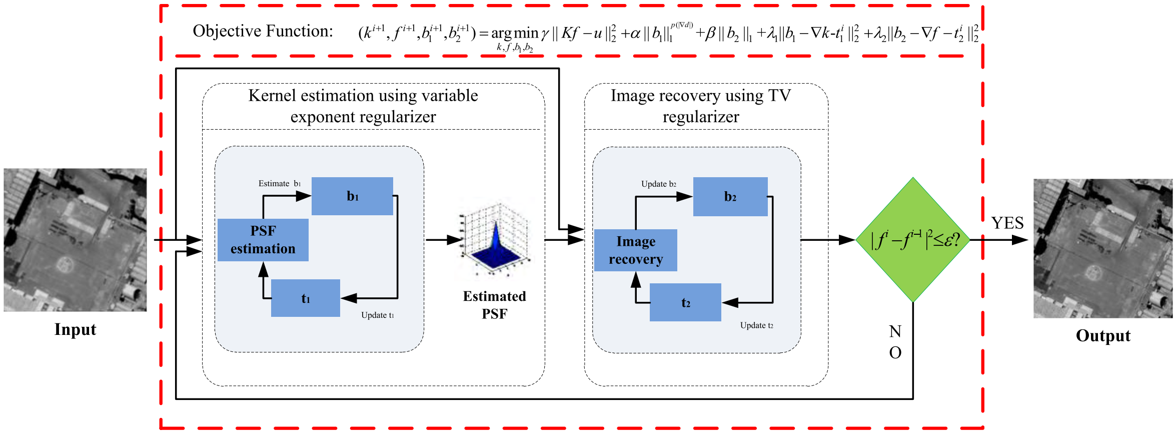

FIGURE 3. Global framework of the proposed method.

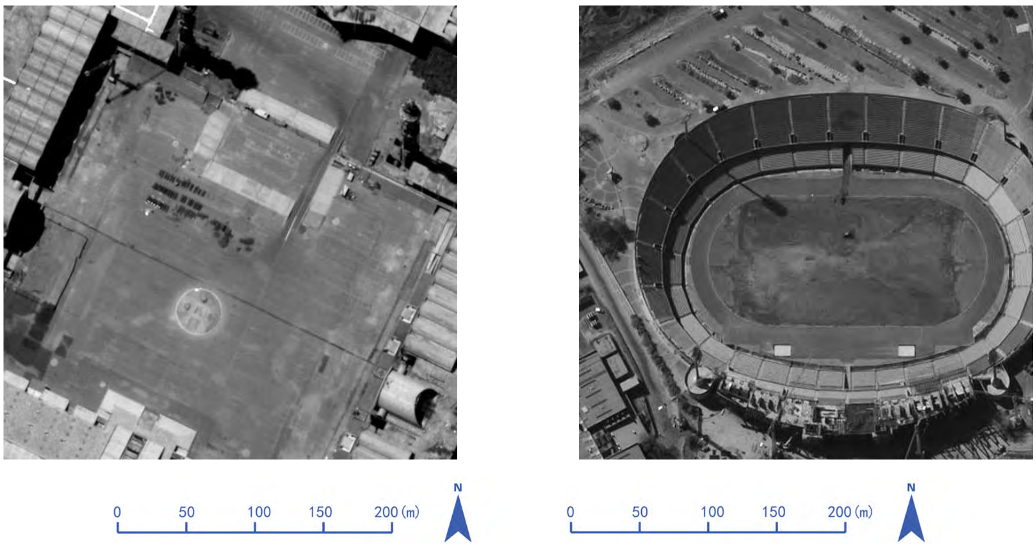

(a) (b)

FIGURE 4. Preprocessed test images for simulated experiments.

TABLE 1. Parameter choices for the simulation experiments.

PSF type	Parameters				
	γ	α	β	λ_1	λ_2
Gaussian PSF	1	100	6.25×10^{-4}	200	1.25×10^{-3}
motion PSF	1	10	6.25×10^{-4}	200	1.25×10^{-3}
disk PSF	1	100	6.25×10^{-4}	200	1.25×10^{-3}
composite PSFs	1	100	6.25×10^{-4}	200	1.25×10^{-3}

If aircraft motion is the main reason, the PSF would be piecewise constant and sparse. In reality, all three factors contribute to degradation, and the PSF is a convolution of the three forms. Thus, using a simple prior will not provide satisfactory results. However, most existing blind restoration methods require a hard decision on the PSF's structure (usually Gaussian type) by adding simple priors to the algorithms, which restricts algorithm flexibility.

In our study, we concentrated on the diversity of different PSF types. We proposed a new blind deconvolution

TABLE 2. Peak signal to noise ratio (RSNR), structural similarity (SSIM), and Q metric for the simulation experiments.

Images	Indexes	PSF type	Degraded	NSBD	HMBD	TVBD	Proposed Newton	Proposed LUT
Figure 4a	PSNR	Gaussian	39.8513	40.1515	44.5239	46.1368	**46.6250**	46.6248
	SSIM		0.9595	0.9628	0.9933	0.9921	**0.9951**	0.9951
	Q		0.0714	0.0620	0.0769	**0.0844**	0.0823	0.0823
	PSNR	Motion	39.5404	42.3132	45.3492	**46.2256**	46.1785	46.1767
	SSIM		0.9512	0.9856	0.9924	**0.9927**	**0.9927**	0.9926
	Q		0.0685	0.0712	0.0734	**0.0862**	0.0861	0.0861
	PSNR	Disk	39.8163	40.0011	41.3274	**44.2417**	44.1344	44.1326
	SSIM		0.9239	0.9546	0.9858	**0.9932**	0.9924	0.9923
	Q		0.0699	0.0744	0.0822	0.0923	**0.1111**	0.1111
	PSNR	Gaussian + Motion	35.5630	39.3712	44.8041	43.3341	**46.7181**	46.7174
	SSIM		0.9566	0.9409	0.9932	0.9921	**0.9933**	0.9932
	Q		0.0728	0.0665	0.0691	0.0827	**0.0852**	0.0851
	PSNR	Gaussian + Disk	36.8776	38.0644	42.5642	42.6872	**43.3022**	43.3009
	SSIM		0.9548	0.9623	0.9880	0.9902	**0.9934**	0.9934
	Q		0.0719	0.0798	0.0811	0.0821	**0.0851**	0.0851
	PSNR	Gaussian + Motion + Disk	36.7207	39.9822	46.0543	45.1092	**46.7040**	46.7040
	SSIM		0.9529	0.9612	0.9912	0.9905	**0.9935**	0.9935
	Q		0.0710	0.0555	0.0753	0.0863	**0.0875**	0.0874
Figure 4b	PSNR	Gaussian	40.5790	40.7262	44.3691	45.5824	**45.8469**	45.8459
	SSIM		0.9185	0.9196	0.9798	0.9887	**0.9897**	0.9896
	Q		0.0777	0.1046	0.0935	0.1048	**0.1061**	0.1061
	PSNR	Motion	40.5025	40.0311	41.8559	**45.4559**	45.3475	45.3462
	SSIM		0.8925	0.8766	0.9408	**0.9797**	0.9791	0.9789
	Q		0.0826	0.0786	0.0908	**0.1126**	**0.1126**	0.1124
	PSNR	Disk	40.5257	41.1807	44.0017	**45.8610**	45.0714	45.0707
	SSIM		0.9153	0.9243	0.9741	**0.9872**	0.9831	0.9831
	Q		0.0755	0.1100	0.1175	0.1161	**0.1205**	0.1204
	PSNR	Gaussian + Motion	31.3635	38.7657	41.1686	37.4918	**43.4571**	43.4562
	SSIM		0.8888	0.9723	0.9768	0.9705	**0.9802**	0.9801
	Q		0.0967	0.1002	0.1031	0.1025	**0.1046**	0.1045
	PSNR	Gaussian + Disk	31.2876	33.9630	44.0981	43.0242	**44.2656**	44.2648
	SSIM		0.8873	0.9436	0.9789	0.9770	**0.9776**	0.9774
	Q		0.0915	0.0964	0.0974	0.1061	**0.1078**	0.1078
	PSNR	Gaussian + Motion + Disk	31.2802	38.2649	42.4007	43.1236	**44.0349**	44.0338
	SSIM		0.8831	0.9346	0.9779	0.9813	**0.9822**	0.9822
	Q		0.0890	0.0989	0.0956	0.1083	**0.1096**	0.1095

model using a variable exponent regularizer to improve kernel structure flexibility. The main advantage of the proposed model was that it could incorporate many PSF types such as motion, uniform, Gaussian, and composite PSFs. We showed theoretically that the existence of a solution of the proposed model was guaranteed. We derived the split Bregman based

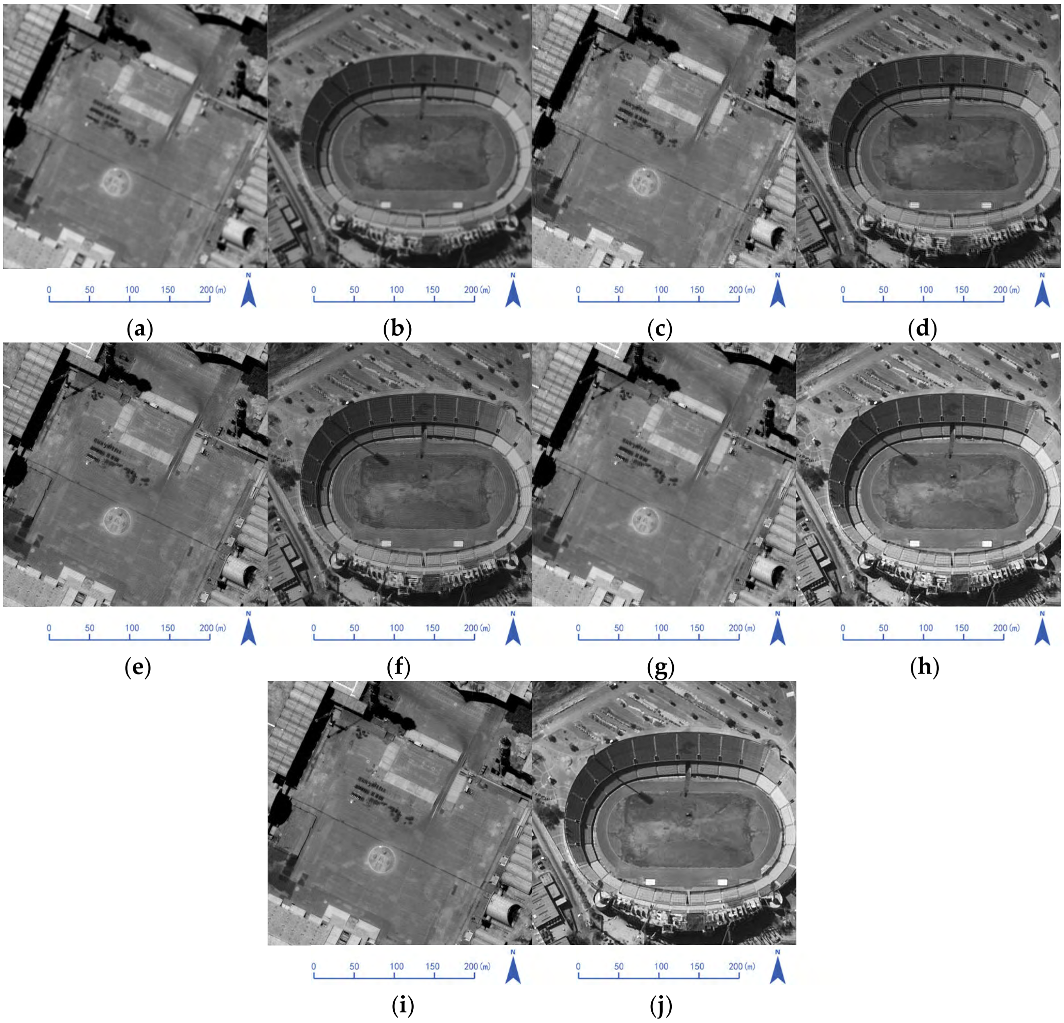

FIGURE 5. Simulation experiment using images degraded by 5 × 5 truncated Gaussian PSF: (a), (b) degraded images; and restored images using (c), (d) NSBD; (e), (f) HMBD; (g), (h) TVBD method; and (i), (j) the proposed method.

alternating minimization, which does not need PSF initialization, to minimize the proposed cost function iteratively.

The rest of the paper is organized as follows. In Section 2, we present the new model. In Section 3, we develop the split Bregman based method to solve the proposed model. In Section 4, we discuss the choice of parameters and compare the proposed method with several state-of-the-art models. In Section 5, we discuss connections with the other methods, convergence analysis of the algorithm and the advantages and disadvantages of the model. In Section 6, we provide our conclusions.

II. BLIND DECONVOLUTION WITH VARIABLE EXPONENT REGULARIZER

One of the biggest challenges in blind restoration is PSF estimation. Actual remote sensing PSFs are often composed of simple PSF types. Composite PSFs have more flexible structures, combining different features of simple PSFs. FIGURE 1 shows three of the most common simple PSFs and three composite PSFs formed by convoluting two or three different PSF types. The Gaussian-disk composite PSF formed by convoluting Gaussian and disk PSFs is similar to Gaussian, but less smooth than pure Gaussian. The Gaussian-motion composite PSF is no longer piecewise constant and the Gaussian-disk-motion composite PSF has no sharp edges.

Conventional blind methods normally employ two distribution priors to model PSF shapes, Gaussian and Laplace distributions, which are equivalent to TV and Tikhonov regularizers. The TV regularizer is a very successful method for piecewise constant PSF restoration because of its crisp edge reconstruction. However, for smooth PSFs, the TV regularizer does not produce satisfactory results [37]. Tikhonov regularization is far superior for smooth PSF reconstruction, but smears edges if the PSF is piecewise constant. Thus, it seems sensible to combine the advantages. The basic concept was to use TV-like regularization near the edges, Tikhonov-like regularization in flat regions, and a compromised regularizer elsewhere as it would provide better smoothness, while still allowing recovery of the sharp edges, thus allowing improved flexibility in PSF structures. For remote sensing images,

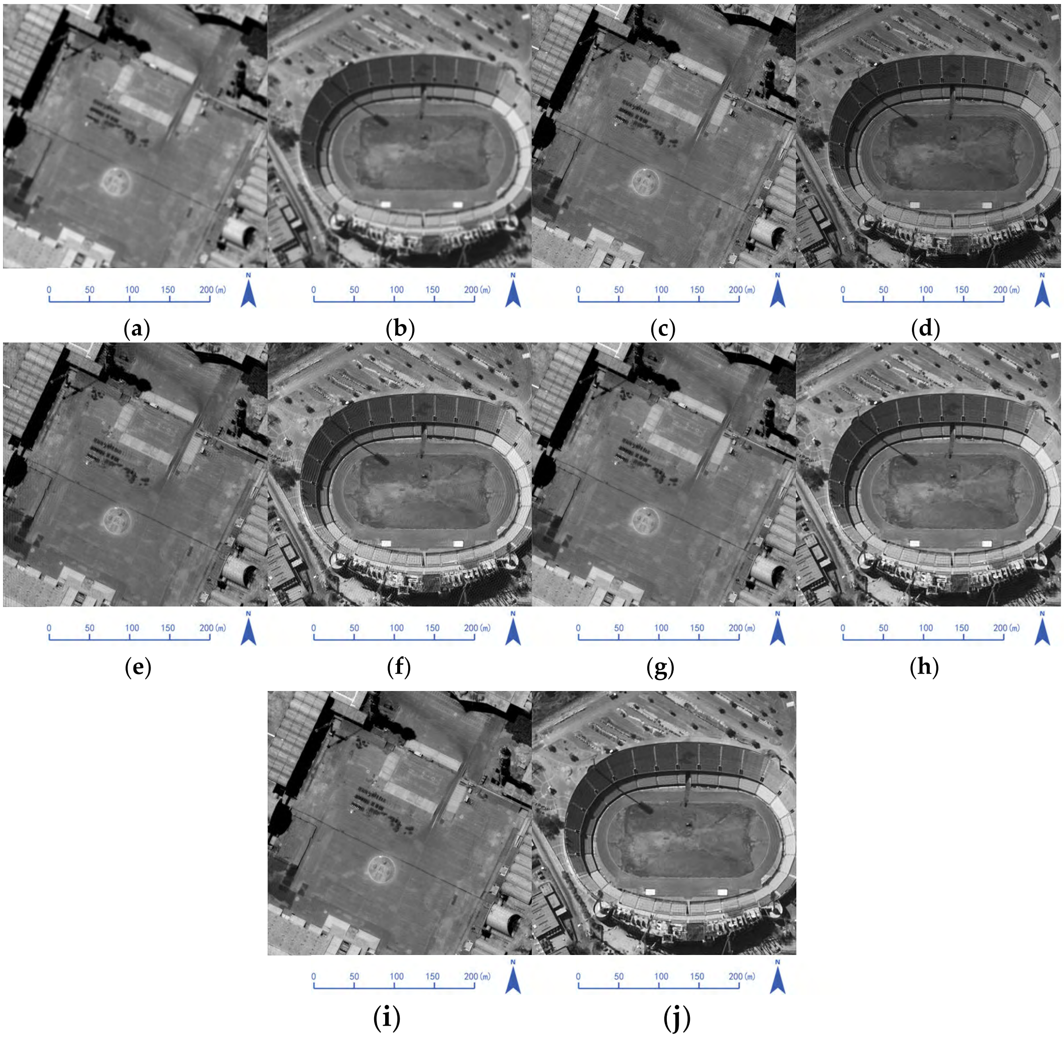

FIGURE 6. Simulation experiment using images degraded using disk PSF: (a), (b) degraded images; and restored images using (c), (d) NSBD; (e), (f) HMBD; (g), (h) TVBD; and (i), (j) the proposed method.

although the main degradation factor is atmospheric turbulence, the PSF is usually a composition of multiple simple PSFs, leading to a less smooth shape than pure Gaussian. The proposed model uses a variable exponent regularizer $R(k)$ for estimating PSF,

$$R(k) = \int |\nabla k|^{p(|\nabla c|)} d\delta$$

where k is the PSF estimation, $|\nabla k| = \sqrt{k_x^2 + k_y^2}$, where k_x and k_y are the partial derivatives. c is the true PSF, which will be discussed in Section 3, and

$$p(s) = 1 + \frac{1}{1 + ts^2} \tag{2}$$

which has the following properties:

1. $p(s)$ is an inversely relation function with respect to s;
2. $p(s)$ ranges from 1 to 2;
3. for edges, i.e., s is large, p tends to 1;
4. for flat regions, i.e., s is small, p tends to 2.

Thus, $|\nabla k|^{p(|\nabla c|)}$ can automatically distinguish different regions and provide different penalty degrees adaptively.

The parameter t can be considered as a threshold. It controls the curve rate of decrease, as shown in Figure 1 for various t. When t is large, TV-like regularization is dominant; whereas if t is small, Tikhonov-like regularization has the leading role in most regions, which would smear edges. Thus, t must be appropriately selected to meet the anticipated requirements.

We formulated the proposed model as

$$\begin{aligned}
&\min_{f,k} J(f, k) \\
&\quad = \min_{f,k} \gamma ||k(x, y) \otimes f(x, y) - u(x, y)||_2^2 \\
&\qquad + \alpha R(k) + \beta \int |\nabla f| d\delta \\
&\qquad \text{subject to } k(x, y) \geq 0, \quad (x, y) \in D, \\
&\qquad\qquad \int_D k(x, y) d\delta = 1, \quad (x, y) \in D, \\
&\qquad\qquad 0 \leq \min(f) \leq f(x, y) \leq \max(f) < \infty, \\
&\qquad\qquad (x, y) \in \Omega,
\end{aligned} \tag{3}$$

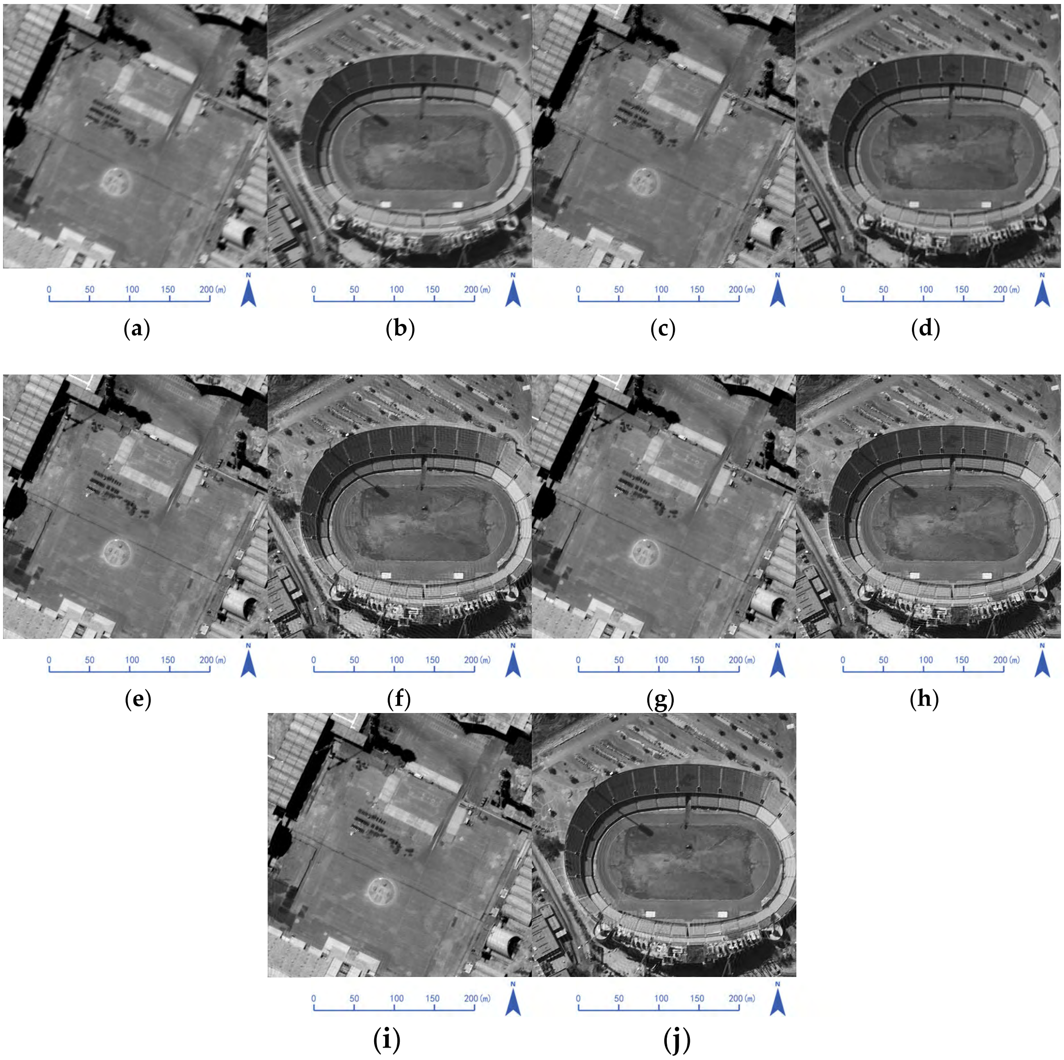

FIGURE 7. Simulation experiment using images degraded using motion PSF: (a), (b) degraded images; and restored images using (c), (d) NSBD; (e), (f) HMBD; (g), (h) TVBD; and (i), (j) the proposed method.

Where γ, α and β are positive constants; and D denotes the PSF support.

Similar regularization has been applied in other fields. Blomgren *et al.* [37] proposed a similar functional for image denoising problems, minimizing

$$E(u) = \int_{\Omega} |\nabla u|^{p(|\nabla u|)} dx$$

where u is the denoised image and $p(\cdot)$ is the decreasing function with $\lim_{s\to 0} p(s) = 2$, $\lim_{s\to\infty} p(s) = 1$. However, since p relies on ∇u, it is difficult to establish the lower semi continuity property of the functional. Chen *et al.* [38] proposed a variable exponent linear growth functional model for image denoising, enhancement, and restoration. Li *et al.* [39] extended this using variable exponent functionals for image denoising problems. Dou *et al.* [40] proposed a variable exponent functional based Retinex model for realistic image rendition.

We show a solution existence for the proposed model.

Theorem 1: Let $\Omega \subset R^2$ be a bounded set, $u \in L^2(\Omega) \cap BV(\Omega), f \in L^2(\Omega) \cap BV(\Omega)$, $||f||_\infty \le ||u||_\infty$; $||\nabla f|| < M$ a.e. on Ω. $k \in W^{1,p(x)}(\Omega) \cap L^1(\Omega)$ is equi-continuous and has a compact support D, $k \ge 0$, $\int_{\Omega} kdx = 1$. Then Equation (3) has the solution pair $(f_*, k_*) \in (L^2(\Omega) \cap BV(\Omega)) \times (W^{1,p(x)}(\Omega) \cap L^1(\Omega))$.

Proof: Please see Appendix A.

III. NUMERICAL IMPLEMENTATION EMPLOYING SPLIT BREGMAN ITERATION

Following the split Bregman framework [41] and alternating minimization algorithm [28], we derived an alternating split Bregman scheme to solve Equation (3). To use Fourier transform, we assumed that both images and PSFs had periodic boundary conditions. To derive the alternating split Bregman algorithm, we introduced two dual variables, b_1 and b_2, to replace ∇k, ∇f respectively and considered the discrete

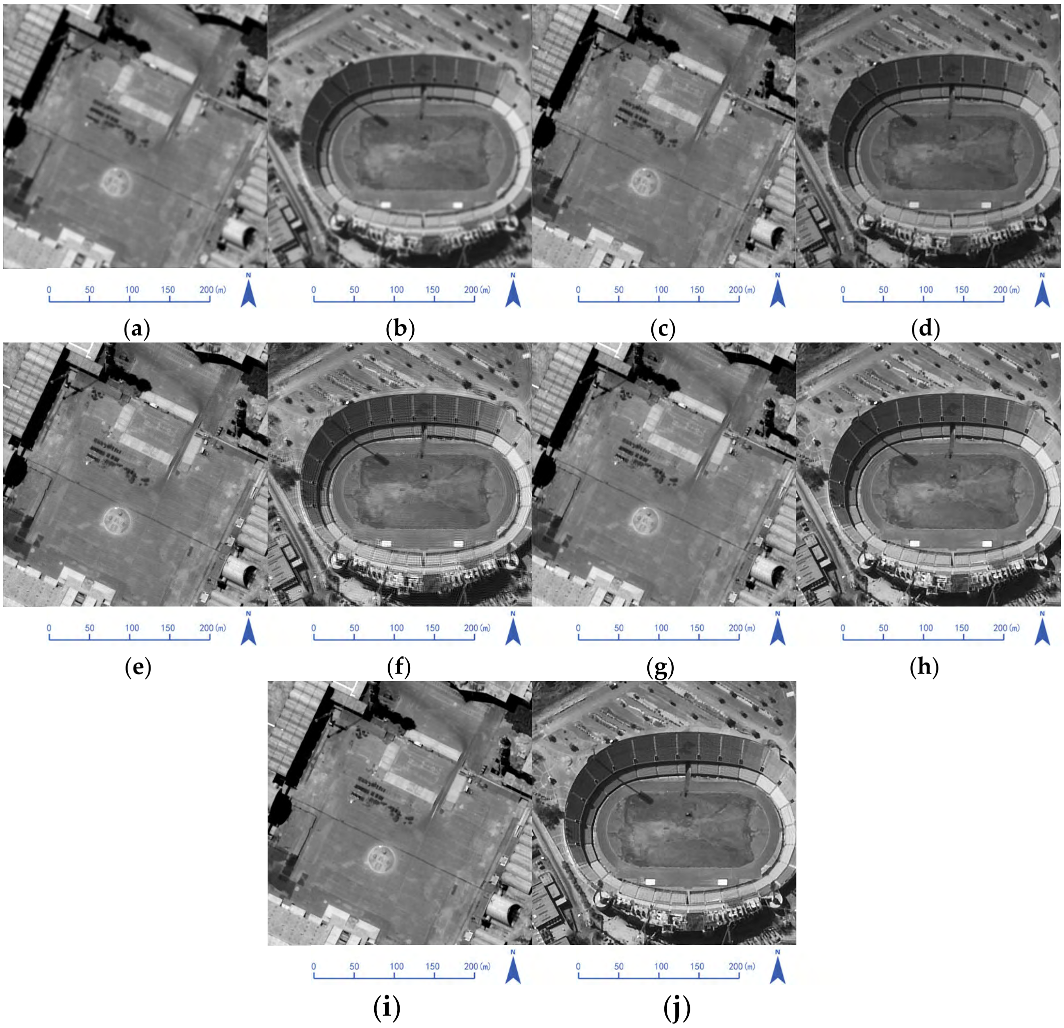

FIGURE 8. Simulation experiment using images degraded using Gaussian-disk PSF: (a), (b) degraded images; and restored images by (c), (d) NSBD; (e), (f) HMBD; (g), (h) TVBD; and (i), (j) the proposed method.

version of Equation (3), yielding the discrete constrained optimization problem

$$\min_{f,K} J(f,K) = \min_{f,K} \gamma\, ||Kf-u||_2^2 + \alpha \sum |b_1|^{p(|\nabla c|)} + \beta \sum |b_2| \tag{4}$$

$$\text{subject to } b_1 = \nabla k, \quad b_2 = \nabla f \tag{5}$$

where f, u, and k denote the unknown sharp image, observed image, and PSF, respectively, in vector form, which are formed by column lexicographical ordering; γ, α, and β are positive constants; K is a block circulant matrix with a circulant block formed by k; $|b| = \sqrt{b_1^2 + b_2^2}$, where all the operation is element-wise and $b = (b_1, b_2)$ where b_1 and b_2 are the vectors; $\nabla k = (k_x, k_y)$, $\nabla u = (u_x, u_y)$, in which u_x and u_y (or k_x and k_y) represent the first-order finite difference of u (or k) in the horizontal and vertical directions respectively; p is defined in Equation (2) and $\sum$ denotes the summation taken over all elements of the vector. Using the augmented Lagrangian method, we redefined this model as

$$\min_{f,k} J(f,k) = \min_{f,k} \gamma ||Kf-u||_2^2 + \alpha \sum |b_1|^{p(|\nabla c|)} + \beta \sum |b_2| + \lambda_1 ||b_1 - \nabla k||_2^2 + \lambda_2 ||b_2 - \nabla f||_2^2 \tag{6}$$

where λ_1 and λ_2 are positive parameters. Like the split Bregman iteration, the proposed iteration scheme is

$$(k^{i+1}, f^{i+1}, b_1^{i+1}, b_2^{i+1}) = \arg\min_{k,f,b_1,b_2} \gamma ||Kf-u||_2^2 + \alpha \sum |b_1|^{p(|\nabla c|)} + \beta \sum |b_2| + \lambda_1 ||b_1 - \nabla k - t_1^i||_2^2 + \lambda_2 ||b_2 - \nabla f - t_2^i||_2^2 \tag{7}$$

$$t_1^{i+1} = t_1^i + \nabla k^{i+1} - b_1^{i+1} \tag{8}$$

$$t_2^{i+1} = t_2^i + \nabla f^{i+1} - b_2^{i+1} \tag{9}$$

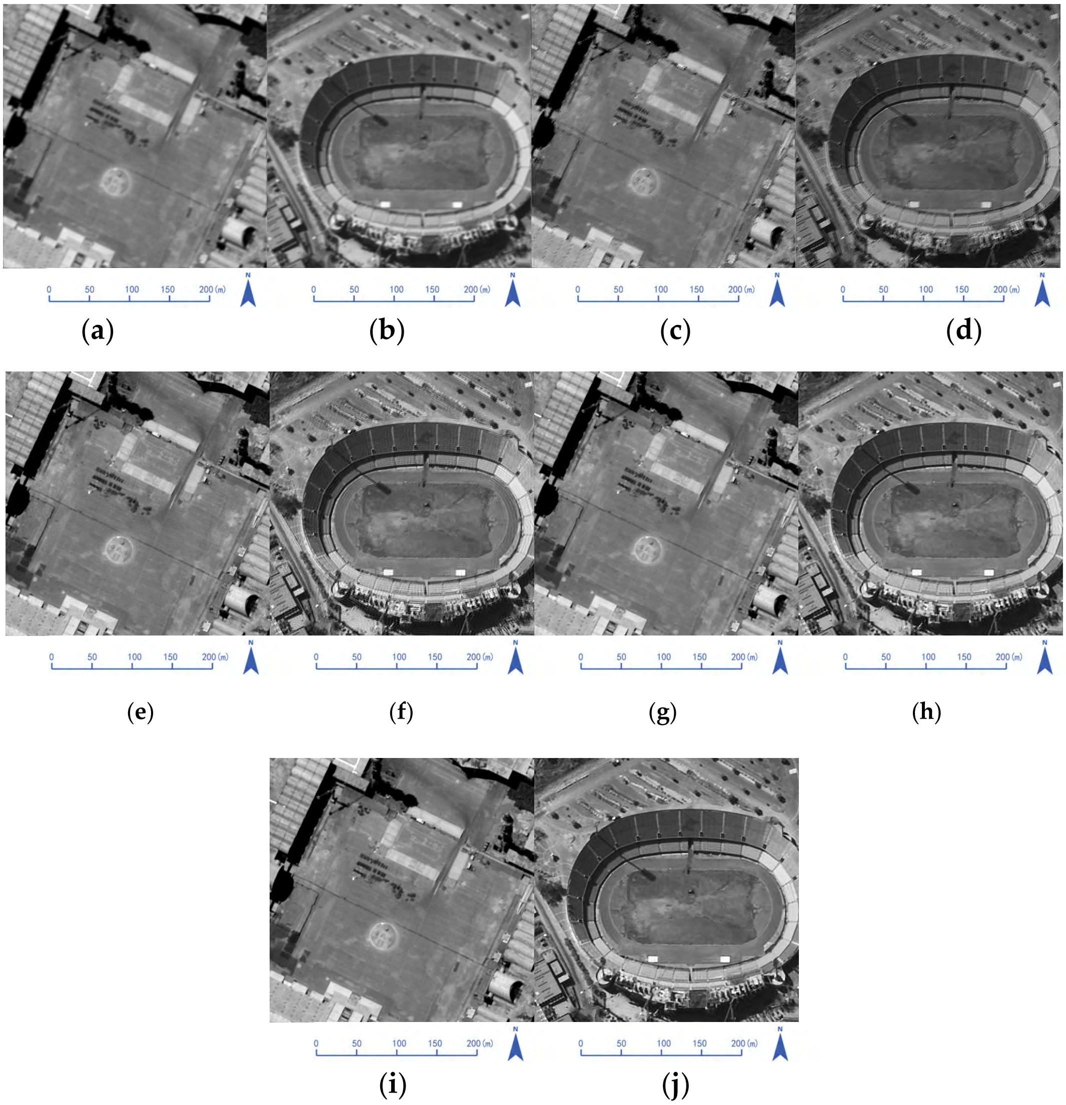

FIGURE 9. Simulation experiment using images degraded using Gaussian motion PSF: (a), (b) degraded images; and restored images using (c), (d) NSBD; (e), (f) HMBD; (g), (h) TVBD; and (i), (j) the proposed method.

Using the alternating minimizing algorithm, the joint minimizing Equation (7) can be solved by decoupling into several subproblems:

1. Calculate the k subproblem with fixed b_1, t_1 and f:

$$k^{i+1} = \arg\min_{k} \gamma ||F^i k - u||_2^2 + \lambda_1 ||b_1^i - \nabla k - t_1^i||_2^2 \tag{10}$$

where F^i is a block circulant matrix with a circulant block generated by image f^i. The optimal k^{i+1} satisfies

$$\gamma (F^i)^T (F^i k^{i+1} - u) - \lambda_1 \Delta k^{i+1} + div(b_1^i - t_1^i) = 0 \tag{11}$$

Where T, Δ and div are the conjugate, Laplace and divergence operators respectively. Equation (11) can be computed efficiently using fast Fourier transform (FFT),

$$k^{i+1} = FFT^{-1}\left(\frac{FFT((F^i)^T u - \frac{\lambda_1}{\gamma} div(b_1^i - t_1^i))}{FFT((F^i)^T F^i - \frac{\lambda_1}{\gamma}\Delta)}\right) \tag{12}$$

Then some constraints of model (3) are added to obtain physical solutions. Note that as the support size of true PSF is usually unknown, the size of the initial support D must be set no less than the true support.

2. Calculate the b_1 subproblem with fixed k^{i+1}, t_1, and f:

$$b_1^{i+1} = \arg\min_{b_1} \alpha \sum |b_1|^{p(|\nabla c|)} + \lambda_1 ||b_1 - \nabla k^{i+1} - t_1^i||_2^2 \tag{13}$$

The corresponding Euler–Lagrangian equation system is

$$\alpha p(|\nabla c|) |b_1|^{p(|\nabla c|) - \frac{1}{2}} b_1 + 2\lambda_1 (b_1 - \nabla k^{i+1} - t_1^i) = 0 \tag{14}$$

Let $b_1 = (b_{11}, b_{12})$ and $t_1 = (t_{11}, t_{12})$, then Equation (14) becomes

$$\begin{cases} (a + 2\lambda_1) b_{11} - 2\lambda_1 k_x^{i+1} - 2\lambda_1 t_{11}^i = 0 \\ (a + 2\lambda_1) b_{12} - 2\lambda_1 k_y^{i+1} - 2\lambda_1 t_{12}^i = 0 \end{cases} \tag{15}$$

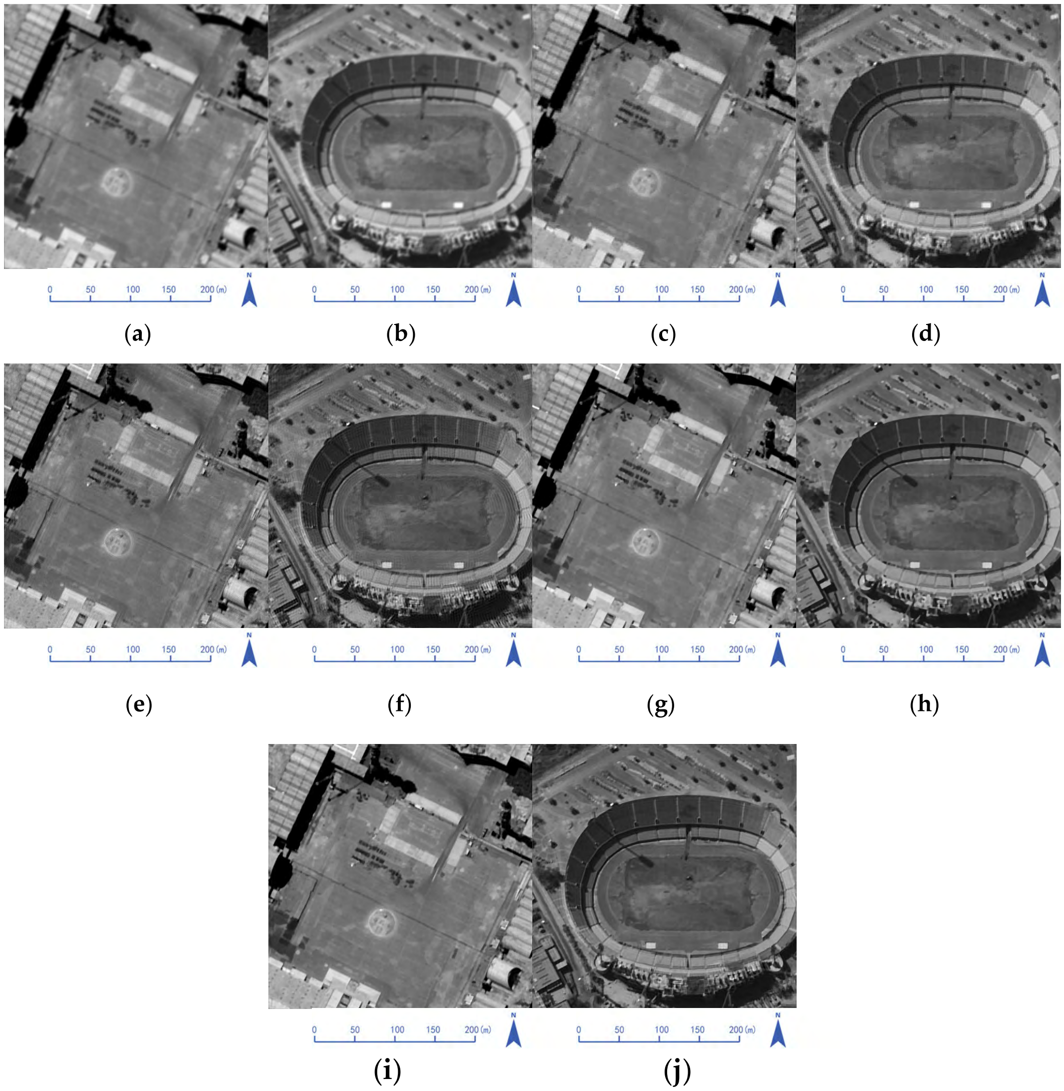

FIGURE 10. **Simulation experiment using images degraded using Gaussian-disk-motion PSF: (a), (b) degraded images; and restored images using (c), (d) NSBD; (e), (f) HMBD; (g), (h) TVBD; and (i), (j) the proposed method.**

where

$$a = \alpha p(|\nabla c|)(b_{11}^2 + b_{12}^2)^{\frac{p(|\nabla c|)}{2}-1} \tag{16}$$

This system cannot be solved explicitly. We describe two approaches to find the numerical solution of Equation (15).

Newton method: A few steps of Newton's method can be used to obtain the numerical solution. From Equation (15), we can deduce that if neither b_{11} nor b_{12} equal zero, then

$$b_{11} = \frac{k_x^{i+1} + t_{11}^i}{k_y^{i+1} + t_{12}^i} b_{12} \tag{17}$$

Newton's algorithm for Equation (15) with respect to b_{11} is
where

$$r = \alpha p(|\nabla c|)(1 + (\frac{k_y^{i+1} + t_{12}^i}{k_x^{i+1} + t_{11}^i})^2)^{\frac{p(|\nabla c|)}{2}-1} \tag{19}$$

Lookup Table Method: Using the above Newton method is time consuming. However, motivated by [46], for a fixed value of p, b_{11} (b_{12}) only depends on $k_x^{i+1} + t_{11}^i$ ($k_y^{i+1} + t_{12}^i$) and α/λ_1, hence we can easily tabulated the solution of Equation (15) in advance to form a lookup table (LUT), which speeds up the computation. We sample 20 numbers uniformly

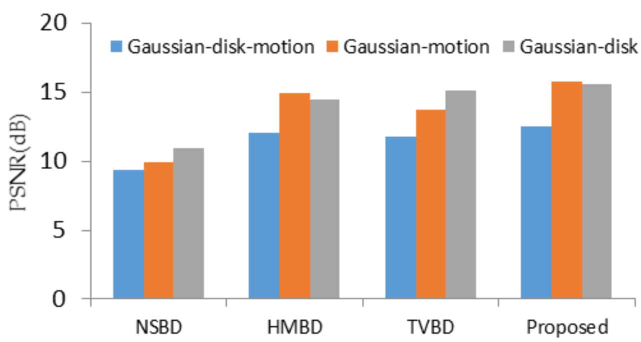

FIGURE 11. **PSNR histogram for various PSFs.**

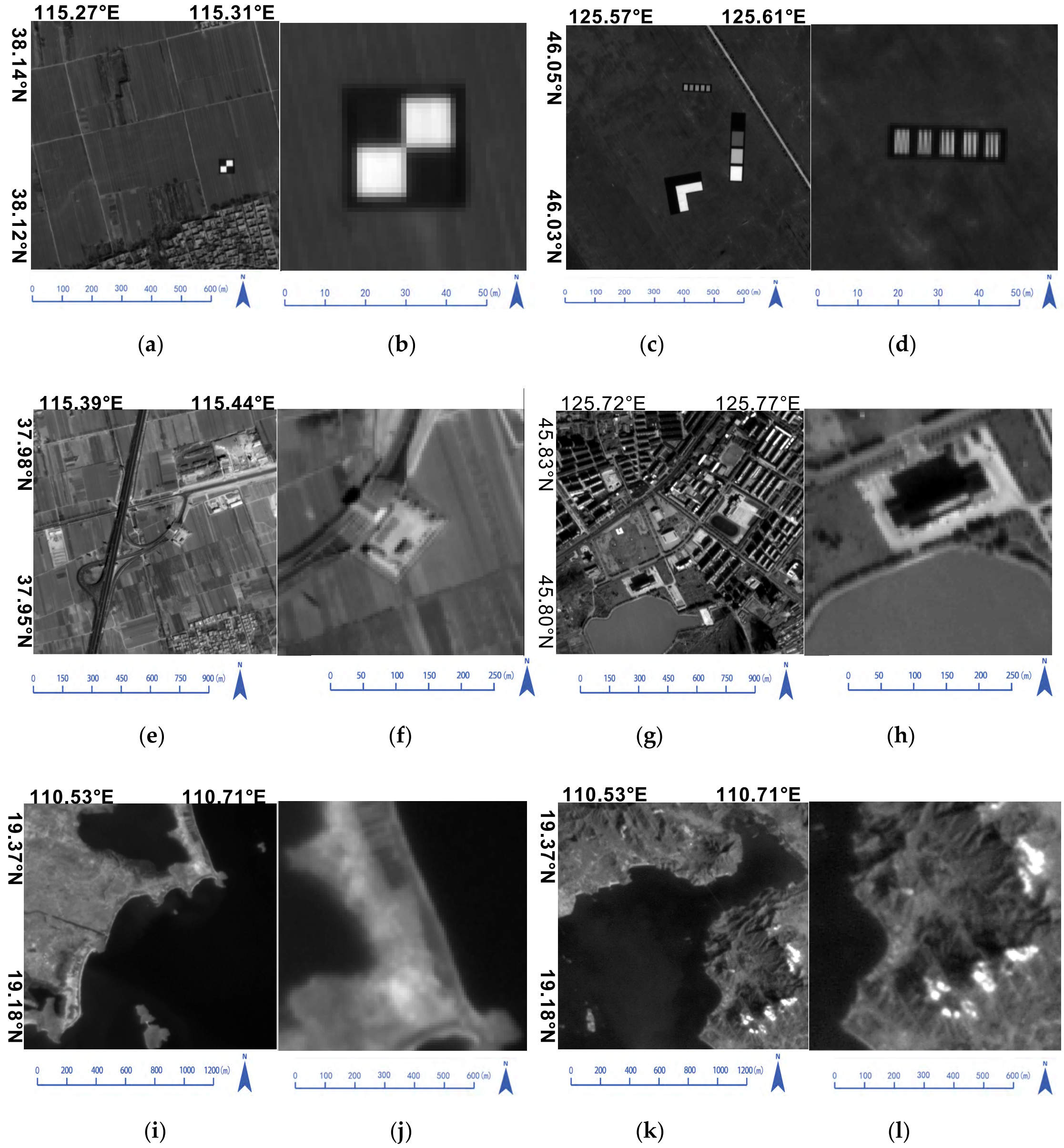

FIGURE 12. The raw sub images cropped from ZY-3 Panchromatic images. (a) Anping City with nadir camera; (b) zoom in; (c) Zhaodong City with nadir camera; (d) zoom in; (e) Anping City with forward camera; (f) zoom in; (g) Zhaodong City with forward camera; (h) zoom in; (i) Pearl River Estuary; (j) zoom in; (k) Hainan Island; (l) zoom in.

Algorithm 1 Newton's Method

While not convergent

$$b_{11}^{j+1} = \mathrm{sign}(k_x^{i+1} + t_{11}^i)\max\{b_{11}^j - \frac{r(b_{11}^j)^{p(|\nabla c|)-1} + 2\lambda_1(b_{11}^j - |k_x^{i+1} + t_{11}^i|)}{(p(|\nabla c|) - 1)r(b_{11}^j)^{p(|\nabla c|)-2} + 2\lambda_1}, 0\} \quad (18)$$

End

from the range of p, from 1 to 2, to make 20 tables. For each sampled number p, b_{11} (b_{12}) is numerically solved for 10,000 and 500 different values of $k_x^{i+1} + t_{11}^i$ ($k_y^{i+1} + t_{12}^i$) and α/λ_1 over the range encountered in our problem ($-1 \leq k_x^{i+1} + t_{11}^i \leq 1, -1 \leq k_y^{i+1} + t_{12}^i \leq 1, 0 \leq \alpha/\lambda_1 \leq 1$). During the computation, we first approximate p of every pixel by the nearest sampled numbers, then use the corresponding off-line tables to solve Equation (15). Although the LUT gives an approximation, it allows b_1 subproblem to be solved very quickly for any $p \in (1, 2]$.

3. Update t_1:

$$t_1^{i+1} = t_1^i + \nabla k^{i+1} - b_1^{i+1} \quad (20)$$

The main problem of this algorithm is that d is unknown in practice. One alternative was to use the last updated k to replace d. In other words, k^{i+1} was used to replace d

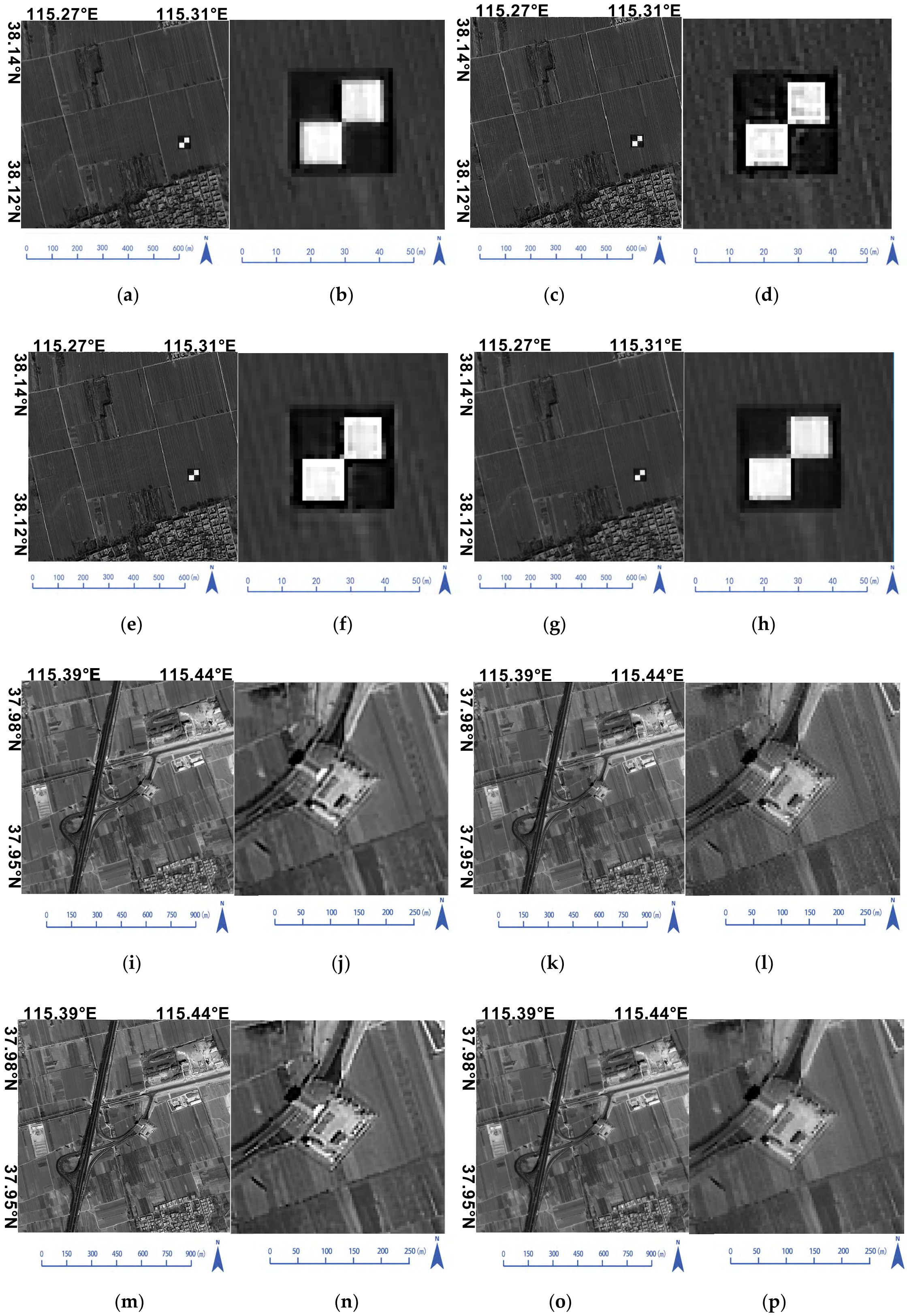

FIGURE 13. Restoration performance using: (a), (i) NSBD and (b), (j) zoomed-in; (c), (k) HMBD and (d), (l) zoomed-in; (e), (m) TVBD and (f), (n) zoomed-in; (g), (o) proposed method and (h), (p) zoomed-in; restored PSF using (q), (u) NSBD; (r), (v) HMBD; (s), (w) TVBD; (t), (x) the proposed method.

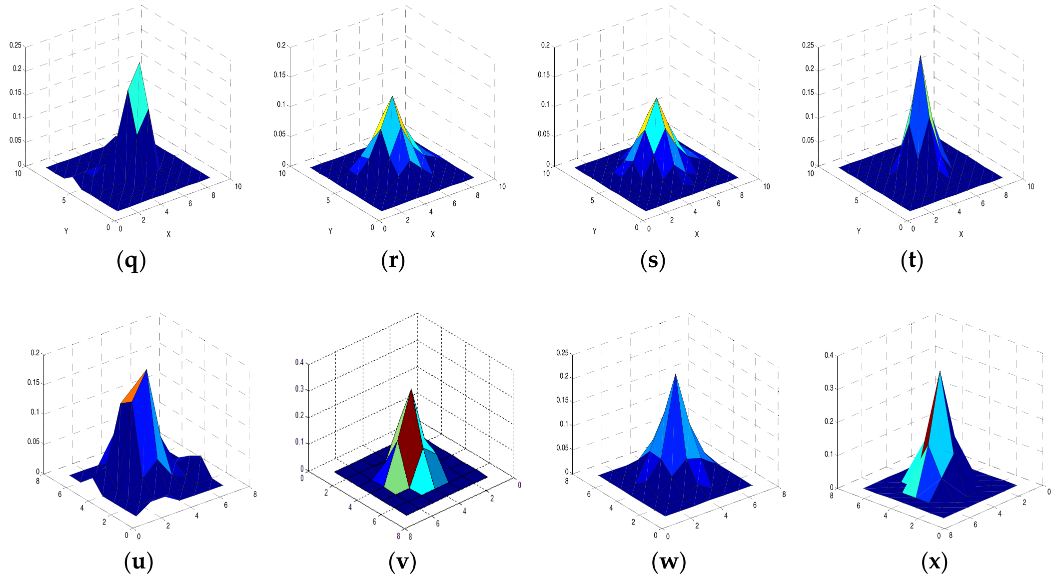

FIGURE 13. ***Continued.*** **Restoration performance using: (a), (i) NSBD and (b), (j) zoomed-in; (c), (k) HMBD and (d), (l) zoomed-in; (e), (m) TVBD and (f), (n) zoomed-in; (g), (o) proposed method and (h), (p) zoomed-in; restored PSF using (q), (u) NSBD; (r), (v) HMBD; (s), (w) TVBD; (t), (x) the proposed method.**

during the ith iteration step. As the exponent changes during computation, it was difficult to prove the overall convergence of the algorithm mathematically. However, as presented in Section 5.1, the algorithm did converge to the desired solution pair.

4. Calculate the f, b_2, t_2 subproblem with fixed b_1, t_1 and k.

When we placed the iterative minimization problem into the framework described in Reference [41] directly, we obtained the algorithm 2, where K^{i+1} is a block circulant matrix with a circulant block generated by k^{i+1} and

$$shrink(x, r) = \frac{x}{|x|}\max(|x| - r, 0).$$

The main advantage of the proposed algorithm is that it does not require an initial estimation of PSF. Figure 3 shows the global framework of the proposed method, and the proposed blind deconvolution algorithm can be summarized as algorithm 3. Readers can read the block diagram and algorithm 3 to understand the global framework.

Algorithm 2 Calculate the Latent Image

While not convergent

For j = 1 to M

$$f^{i+1} = FFT^{-1}\left(\frac{FFT((K^{i+1})^T u - \frac{\lambda_2}{\gamma} div(b_2^i - t_2^i))}{FFT((K^{i+1})^T K^{i+1} - \frac{\lambda_2}{\gamma}\Delta)}\right)$$

$$b_2^{i+1} = shrink(\nabla f^{i+1} + t_2^i, \frac{\beta}{\lambda_2})$$

$$t_2^{i+1} = t_2^i + \nabla f^{i+1} - b_2^{i+1}$$

End

End

IV. PARAMETER SELECTION AND NUMERICAL RESULTS

Here we provide a guideline for parameter selection and present numerical results to demonstrate the efficiency of the proposed model and algorithm. Here we provide a guideline for parameter selection and present numerical results to demonstrate the efficiency of the proposed model and algorithm. In Section 4.1, we present the heuristic choice of parameters, and in Sections 4.2 and 4.3, we used simulated and real data images, respectively, to test the algorithm. Three state-of-the-art blind restoration methods were compared: the normalized sparsity measure (NSBD) [27], Huber-Markov (HMBD) [32], and total variation (TVBD) [21]. In our approach, we compare the performances of the Newton and LUT methods as well.

We tested the proposed algorithm experimentally using different images and PSFs. The code was implemented using MATLAB with machine precision approximately 10^{-16}. For simulated images, we used peak signal to noise ratio (PSNR), structural similarity (SSIM), and the Q metric to evaluate the restored image quality. These indexes were defined as follows.

$$PSNR = 10\log\left(\frac{(2^n - 1)^2}{||f - u||_2}\right) \tag{21}$$

$$SSIM = \frac{(2\mu_u\mu_f + C_1)(2\delta_{fu} + C_2)}{(\mu_f^2 + \mu_u^2 + C_1)(\delta_f^2 + \delta_u^2 + C_2)} \tag{22}$$

$$Q = s_1\frac{s_1 - s_2}{s_1 + s_2} \tag{23}$$

where f and u are the recovered and high quality reference images; μ_f and μ_u represent the mean intensities of f and u,

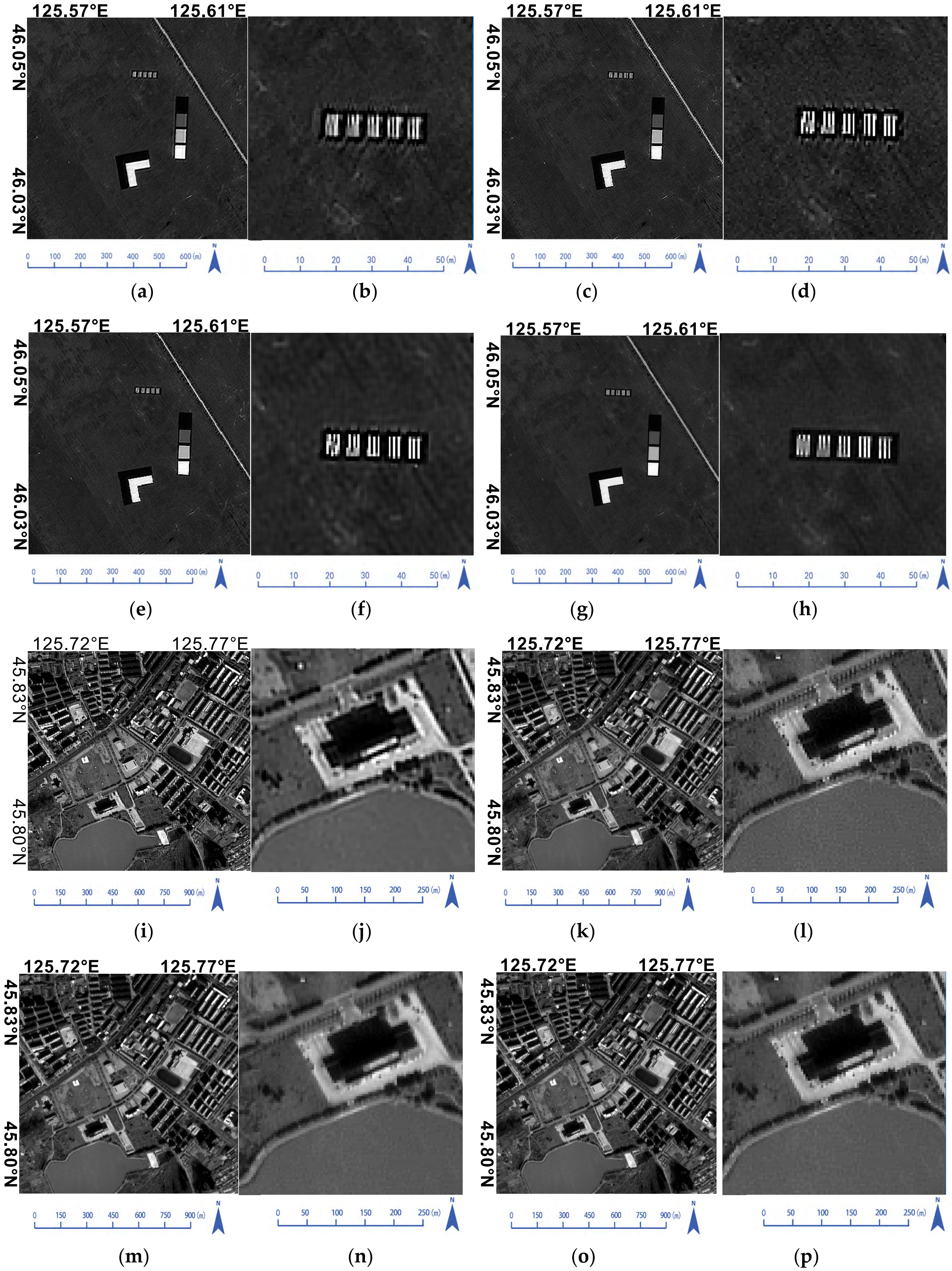

FIGURE 14. Restoration performance using: (a), (i) NSBD and (b), (j) zoomed-in; (c), (k) HMBD and (d), (l) zoomed-in; (e), (m) TVBD and (f), (n) zoomed-in; (g), (o) proposed method and (h), (p) zoomed-in; restored PSF using (q), (u) NSBD; (r), (v) HMBD; (s), (w) TVBD; (t), (x) the proposed method.

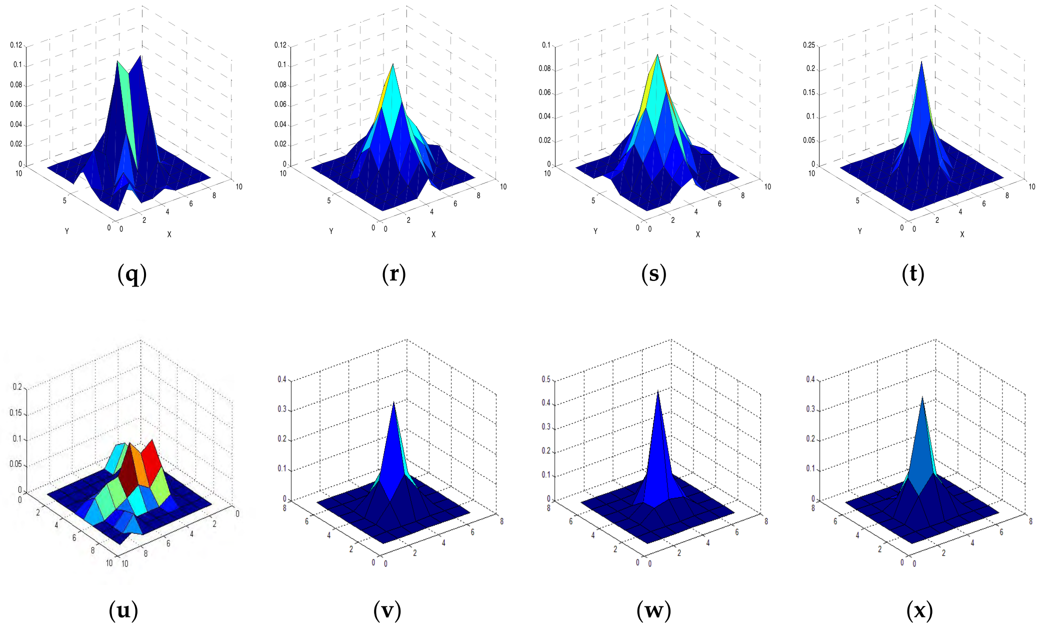

FIGURE 14. ***Continued.*** **Restoration performance using: (a), (i) NSBD and (b), (j) zoomed-in; (c), (k) HMBD and (d), (l) zoomed-in; (e), (m) TVBD and (f), (n) zoomed-in; (g), (o) proposed method and (h), (p) zoomed-in; restored PSF using (q), (u) NSBD; (r), (v) HMBD; (s), (w) TVBD; (t), (x) the proposed method.**

respectively; δ_f, δ_u and δ_{fu} represent the standard deviation of the restored and high quality reference images, and their covariance, respectively; C_1, C_2 are two constants, and s_1 and s_2 are singular values of each 8×8 block in the gradient matrix of the restored image.

For all experiments in this paper, the original image intensities were rescaled into the range [0, 1].

A. PARAMETER SELECTION

There are five parameters in Equation (7), i.e., $\gamma, \alpha, \beta, \lambda_1$ and λ_2. γ measures the fidelity to the original data. Parameters α and β control the PSF and image smoothness, respectively. λ_1 and λ_2 are the penalty term weights which control the similarities between b_1, b_2 and ∇k, ∇f, respectively.

Many recent papers have reported the failure of joint image and PSF estimation, showing that joint estimation methods provided only trivial solutions, i.e., PSF was the delta function and the restored image was the degraded image as both the fidelity and regularizer terms favored a blur solution. Since we wanted non-trivial solutions, the solution pair should be far from the trivial solutions to avoid the undesired local minimum. To achieve this, we imposed an initial strong regularizer to avoid the undesired trivial solution pair.

B. SIMULATED RESTORATION EXPERIMENTS

We tested the proposed algorithm on different kernel types and images, including Gaussian, motion, disk, and composites of these PSFs. Since remote sensing image noise is usually not serious, we added a moderate level of noise to the simulated experiments. The parameters were shown in table 1.

Figure 4 shows two preprocessed 512×512 remote sensing images used in the simulated experiments, cropped from high quality QuickBird products. Figures 5–7 show blurred images generated by a 5×5 truncated Gaussian PSF with standard deviation $= 3$, motion PSF with length 7 and angle 30°, and disk PSF with radius $= 3$, respectively. Blurred images in Figures 8–10 were generated by composite PSFs compounded with the previous PSFs for Gaussian-motion, Gaussian-disk, and Gaussian-disk-motion, respectively. All blur images had white Gaussian noise (WGN) added with variance 0.001. For all experiments, HMBD and TVBD used the Gaussian function as PSF initialization, while NSBD used the horizon bar as PSF initialization. Note that we also used different PSF initialization for the compared methods, but the results remained similar. In contrast, the proposed algorithm didn't require PSF initialization. We have conducted many experiments for all methods and reported the best results.

Table 2 summarizes the PSNR, SSIM, and Q metric of the recovered images for the different methods, including proposed Newton and LUT methods, and PSFs. In general, NSBD performance was limited in certain cases, while the other three methods produced impressive results. The proposed algorithm produced comparable or superior results to the three current state-of-the-art methods in most cases. For Gaussian PSFs, the proposed methods (PSNR and SSIM) were comparable to the other methods. For motion and disk PSFs (which are piecewise constant), TVBD produced better results than the other methods. These outcomes were expected as TV prior favors a piecewise constant solution. However, for composite PSFs, the proposed method outperformed all the other methods in most cases. The main reason

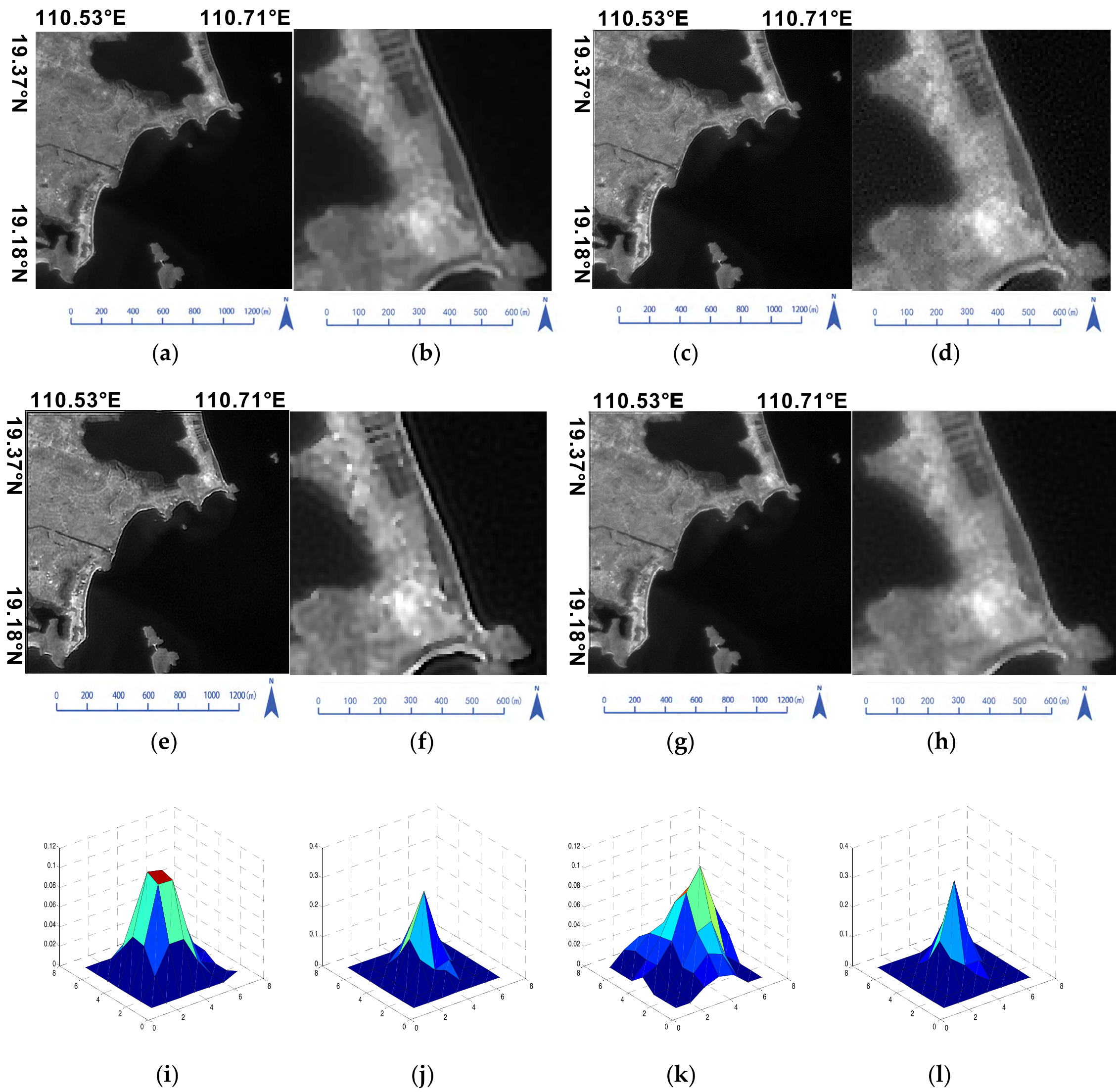

FIGURE 15. Restoration performance using: (a) NSBD and (b) zoomed-in; (c) HMBD and (d) zoomed-in; (e) TVBD and (f) zoomed-in; (g) proposed method and (h) zoomed-in; restored PSF using (i) NSBD; (j) HMBD; (k) TVBD; (l) the proposed method.

is that composite PSFs have new characteristics compared with previous PSFs; and are neither sparse in the gradient domain, nor follow pure Gaussian distribution. Unlike these models, the variable exponent regularizer can adaptively capture the PSF smoothness, thus providing more flexibility and producing superior results. All of the evaluation indexes for the proposed method are almost the same whether we use LUTs or Newton method. However, LUT is about 3 times faster than Newton method, hence in practice the LUT method is preferred.

Figures 5–10 show various visual comparisons of the results. In most cases, NSBD performance was limited, while the three other methods achieved significant visual improvement. For single type kernels, i.e., Gaussian, disk, and motion kernels, HMBD suffered more artifacts in the simulated experiments. These artifacts mainly resulted from the HMRF prior hard threshold, which may mistake some mid-level edges in the images for texture. In contrast, TVBD and the proposed method had few artifacts and similar appearance.

For composite kernels, the proposed method outperformed the other three methods. HMDB and TVBD suffered from ripple (Figure 10) or mosaic (Figures 8–10) effects, while few of these appeared in the proposed method. Since the variable exponent regularizer was more flexible than Tikhonov and TV regularizers, the proposed method could recover more accurate PSFs, thus reducing artifacts in the recovered images.

Figure 11 shows the PSNR histogram of the recovered PSFs for different kernel types. The proposed method achieved the highest PSNR in composite PSF cases, i.e., restored PSFs using the proposed method were closest to ground truth.

Table 3 shows the running time of all the algorithms. The proposed algorithm with LUT is highly competitive compared with the other state-of-the-arts.

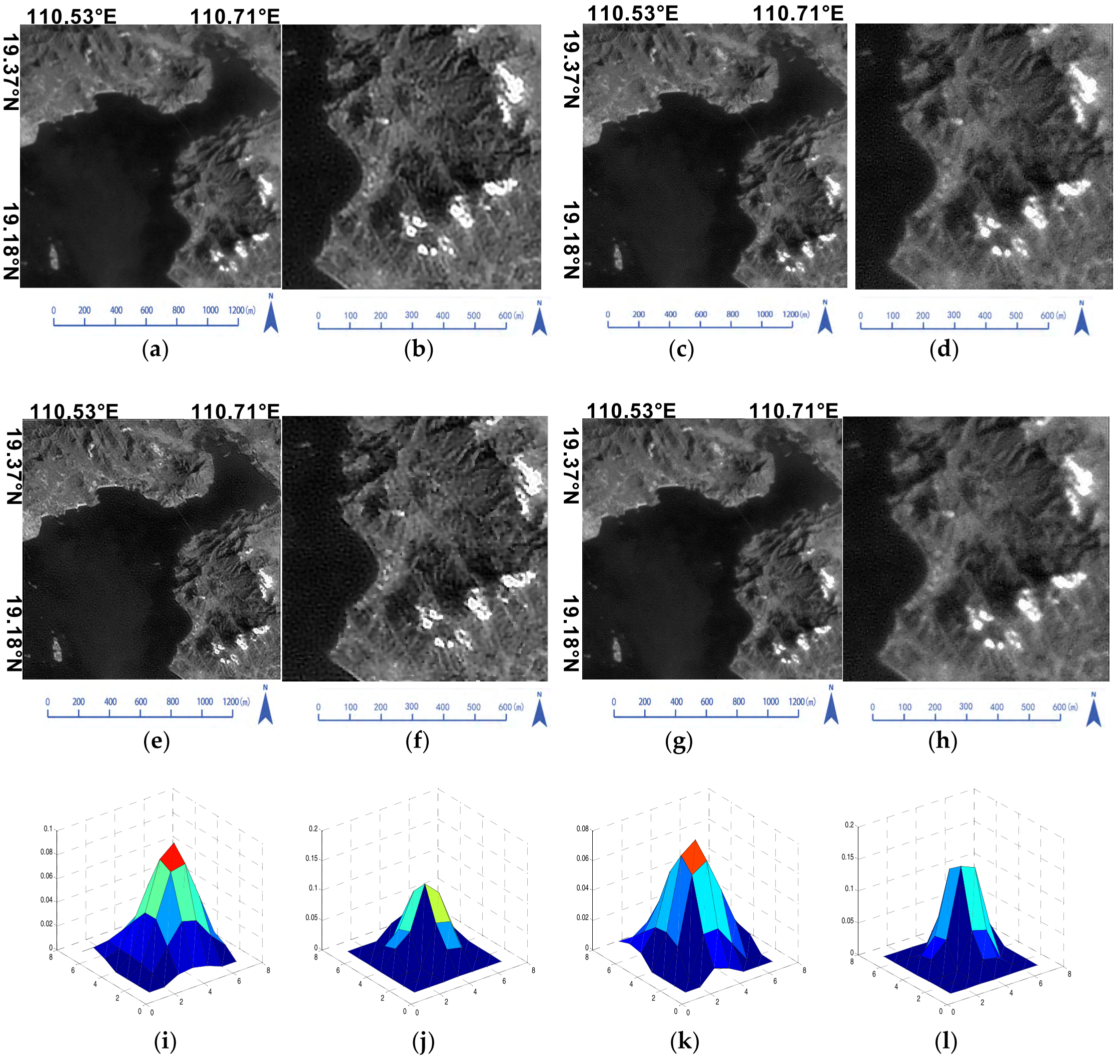

FIGURE 16. Restoration performance using: (a) NSBD and (b) zoomed-in; (c) HMBD and (d) zoomed-in; (e) TVBD and (f) zoomed-in; (g) proposed method and (h) zoomed-in; restored PSF using (i) NSBD; (j) HMBD; (k) TVBD; (l) the proposed method.

TABLE 3. Running time (seconds) comparisons of 5 different methods.

Image Size	NSBD	HMBD	TVBD	Proposed Newton	Proposed LUT
512×512	20.87	183.26	24.77	75.65	24.81

C. RESTORATION OF REAL ZY-3 AND GF-4 PANCHROMATIC IMAGE

The Zi Yuan 3 (ZY-3) cartographic satellite, which was launched on 9 January 2012, is China's first civil high resolution stereo mapping satellite. It carries four optical cameras: three panchromatic time delay integration CCD (TDI-CCD) cameras in the nadir, forward, and afterward views and an infrared multispectral scanner [43]. The nadir (forward) camera has a resolution of 2.1 (3.5) m, a swath width of 50 (52) km, and an on-orbit MTF value at the Nyquist frequency tested of more than 0.12 (0.16). The Gao Fen 4 (GF-4) satellite, launched in Xichang Satellite Launch Center on December 29, 2015, is the first geosynchronous orbit remote sensing satellite in China and equipped with one stare camera with resolution of 50m visible light/400m medium wave infrared ray and swath of over 400km [45].

We tested six real panchromatic images, four from ZY-3 nadir (Figure 12(a), (c)) and forward (Figure 12(e), (g)) cameras, and the other two (Figure 12(i), (k)) from GF-4 satellite. The four images of ZY-3 were acquired on 18 February 2012 (Figure 12(a), (c)) and 13 September 2013 (Figure 12(e), (g)), in Anping and Zhaodong City, Hebei and Heilongjiang Province, and the two test images of GF-4 were acquired on 26 January 2017 (Figure 12(i)) and 20 August 2013 (Figure 12(k)), in Pearl River Estuary and Hainan Island. All of them were level-1 data. Since all the full raw panchromatic images were very large, we cropped six 400×400 sub-images, which contain the calibration targets or other representative features.

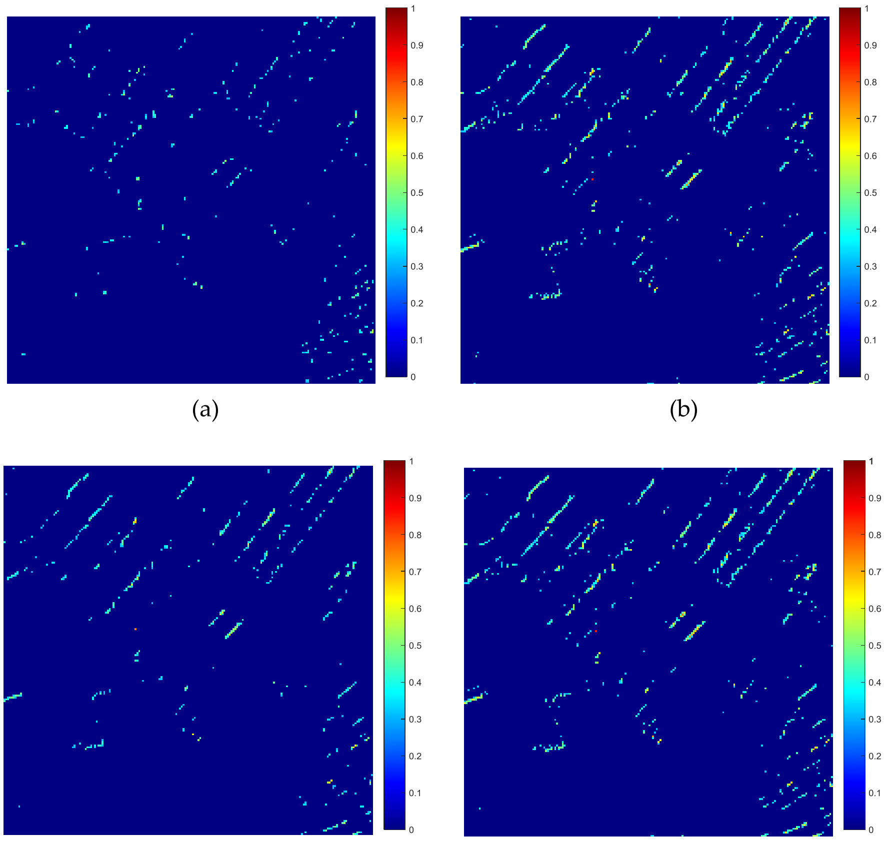

FIGURE 17. Residual images of bottom right part of Figure 12 (g) : (a) NSBD; (b) HMBD; (c) TVBD; (d) the proposed method.

Figures 13–16 show the restored images and restored PSFs. All methods improved visual quality over the raw images; however, the zoomed-in portions of the restored images showed that the proposed method produced less disorder and noise around the calibration target and the representative features, while the other three methods introduced noise or disorder. The restored PSFs showed that they were not purely Gaussian, but more like Gaussian-disk PSFs. Figure 17 shows the comparisons of residual image of the bottom right part in Figure 12 (g). We see that the residual images of NSBD and TVBD have fewer details than those of HMBD and the proposed method, while the residual images of the proposed method contain less noise (see the isolate points of residual images) than that of HMBD.

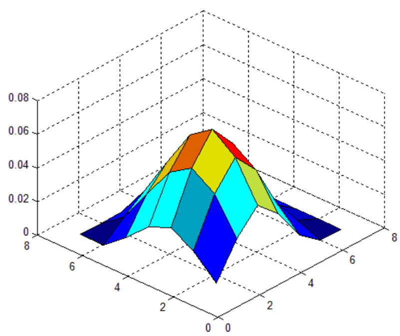

FIGURE 18. The PSF estimation of the first iteration.

V. DISCUSSION

A. CONNECTION AND COMPARISONS WITH EXISTING METHODS

Our objective was to develop a more general and flexible regularizer for estimating PSF from a single degraded remote sensing image. Most existing blind restoration models for remote sensing images, such as the knife edge model [22] and pulse model [24], assumes that the remote sensing images are degraded due to atmosphere turbulence, i.e., the PSF is Gaussian function. If we set $t = 0$ in p, the proposed variable exponent regularizer would degrade to the Tikhonov regularizer, which is equivalent with the above-mentioned models. Thus, the proposed model can be considered as the generalization of the existing models.

Compared to existing methods, we included other degradation factors such as out of focus lens and motion into consideration. The proposed variable exponent regularizer allowed more flexibilities of PSFs, thus could estimate composite PSFs more accurately. In Section 4, we used both

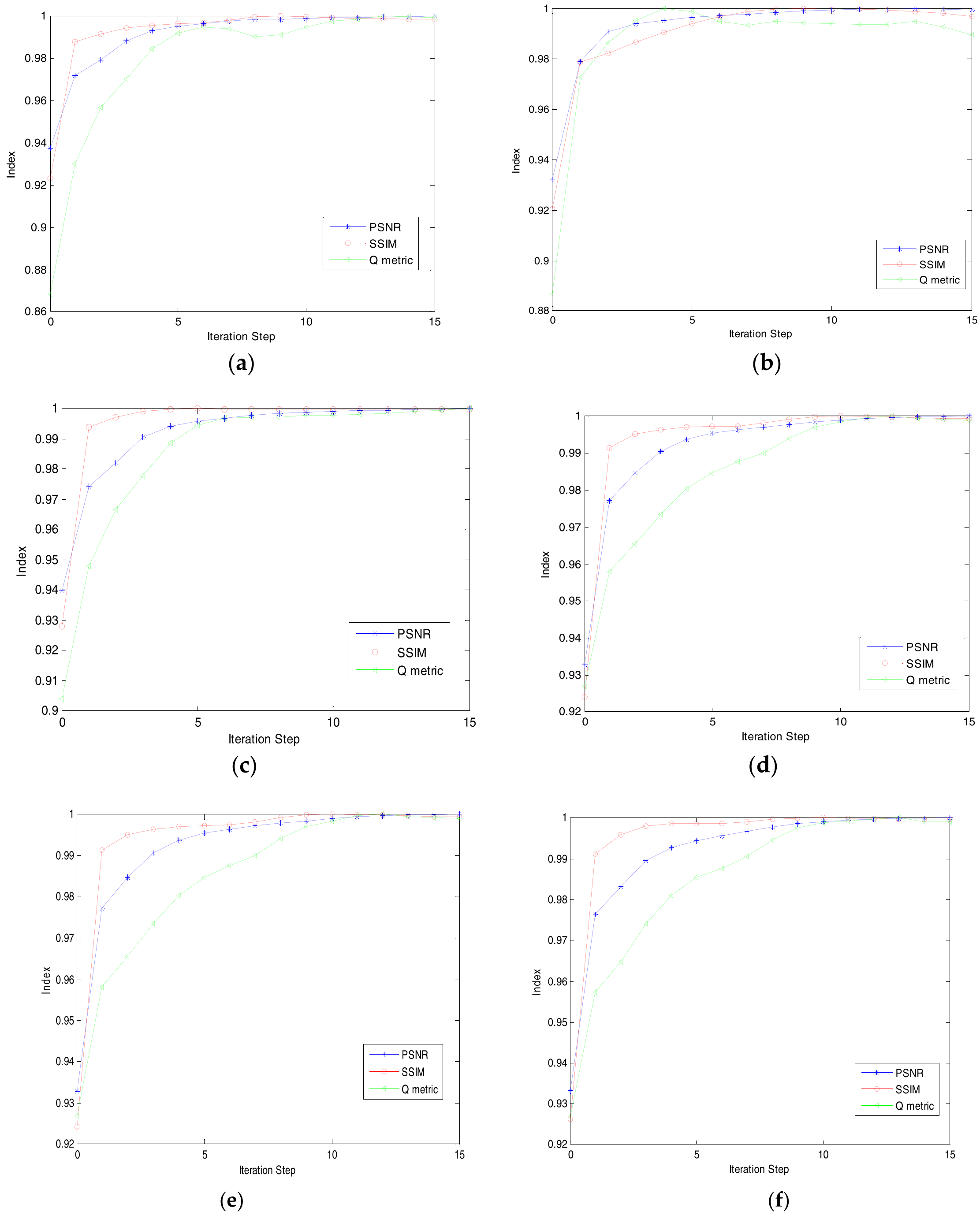

FIGURE 19. Evolution of PSNR, SSIM and Q metric with iteration for different PSF types: (a) Gaussian; (b) motion; (c) disk; (d) Gaussian-motion; (e) Gaussian-disk; and (f) Gaussian-motion-disk.

simulated and real blurred remote sensing images to validate the efficiency of the proposed model. For simple PSFs in simulated experiments, i.e., Gaussian, disk and motion PSFs, the proposed model achieved highly competitive performances in comparison with the other blind restoration methods [21], [27], [32]. For composite PSFs, i.e., Gaussian-disk, Gaussian-Motion and Gaussian-disk-motion PSFs, the proposed model outperformed the other state-of-the-arts in both visual and quantitative assessment, thus validating the efficiency of the proposed model. The real data experiments using raw ZY-3 and GF-4 panchromatic images further validated the effectiveness of the proposed model, which performed well in all experiments. In these experiments, the results of NSBD were the worst in the most of cases, because it used the sparse regularizer to model PSFs, which is incompatible with remote sensing images; the other three

Algorithm 3 Overall Algorithm

1: Initialize: $f^0 = u$, $i = b_1^0 = b_2^0 = t_1^0 = t_2^0 = 0$ and support size of PSF

2: While $|f^i - f^{i-1}|^2 \leq \varepsilon$

3: For j = 1, 2, ... do

$$k^{i+1} = FFT^{-1}\left(\frac{FFT((F^i)^T u - \frac{\lambda_1}{\gamma} div(b_1^i - t_1^i))}{FFT((F^i)^T F^i - \frac{\lambda_1}{\gamma}\nabla)}\right);$$

Impose constraints on k^{i+1};

Solve b_1^{i+1} using Newton or LUT method;

$$t_1^{i+1} = t_1^i + \nabla k^{i+1} - b_1^{i+1}$$

End

4: For j = 1, 2, ... do

$$f^{i+1} = FFT^{-1}\left(\frac{FFT((K^{i+1})^T u - \frac{\lambda_2}{\gamma} div(b_2^i - t_2^i))}{FFT((K^{i+1})^T K^{i+1} - \frac{\lambda_2}{\gamma}\nabla)}\right)$$

$$b_2^{i+1} = shrink(\nabla f^{i+1} + t_2^i, \frac{\beta}{\lambda_2})$$

$$t_2^{i+1} = t_2^i + \nabla f^{i+1} - b_2^{i+1}$$

End

$i = i + 1$;

5: End

methods achieved impressive results. TVBD used TV regularizer to model PSFs, but TV is valid only for piecewise constant PSFs. HMBD method used Huber Markov prior to model both PSFs and images. Huber Markov prior ρ_a also combined the advantages of TV regularizer and Tikhonov regularizer via a hard threshold a:

$$\rho_a(|\nabla f|) = \begin{cases} |\nabla f|^2, & |\nabla f| \leq a \\ 2a|\nabla f| - a^2, & |\nabla f| > a \end{cases}$$

The hard threshold combination may be not the best choice because it may mistake some less smooth regions in PSFs and lead to the piecewise constant like PSFs. However variable exponent regularizer used the compromised regularizer to handle mid-level smooth regions, leading to the more robust results.

While other existing algorithms for remote sensing images are sensitive to the initial PSF [22], the proposed algorithm does not require PSF initialization. In fact, the proposed algorithm used a Gaussian like PSF as the initialization, because the split Bregman algorithm used the Tikhonov regularizer for the first iteration, making the shape of PSF like a Gaussian function, of which Figure 18 shows an example. In addition, though the exponent changed during computation, the algorithm ultimately converged to the desired solution pair. Figure 19 shows the evolution curves of the PSNR, SSIM and Q metric with iterations for different PSF types, where the index values have been normalized to assist visualization. All indexes converged within 15 iterations, indicating the robustness of the proposed algorithm.

B. LIMITATIONS AND FUTURE WORK

The main limitation is that though we formally proved the solution existence of the proposed model, the proof of the proposed algorithm is difficult since the exponent changed during the computation. Thus, we will investigate this as future work.

VI. CONCLUSIONS

We proposed a new blind deconvolution model using a variable exponent regularizer. The main advantage of the proposed model was that it could incorporate many PSF types, such as motion, uniform, Gaussian and composite PSFs. A split Bregman based alternating minimization method was employed to minimize the proposed cost function iteratively. Furthermore, the proposed algorithm did not require PSF initialization. The algorithm converged within 15 loops in all experiments.

In our work, both simulated and real blurred remote sensing images were tested. Experimental results demonstrated that for simple PSFs, i.e., Gaussian, disk, and motion, the proposed model achieved highly competitive results with other state-of-the-art methods; for composite PSFs, the proposed model outperformed the other methods. The real data experiments with ZY-3 and GF-4 panchromatic images further demonstrated the effectiveness of the proposed method.

We formally proved the solution existence of the proposed model, but evidence of the proposed algorithm was difficult since the exponent changed during the computation. Thus, this will be investigated as a future research area.

APPENDIX

Appendixes, if needed, appear before the acknowledgment.

Proof of Theorem 1. We first present some preliminaries for variable exponent space and its properties, following [39] and [43].

Definition 1 (Variable Exponent Spaces): Let Ω be a bounded open set with a Lipschitz boundary and $p(x) : \Omega \to [1, +\infty)$ a measurable function, with the family of all measurable functions on Ω being $P(\Omega)$. We define a functional, which is also called modular,

$$Q_{p(x)}(u) = \int_\Omega |u|^{p(x)} dx$$

and a norm,

$$||u||_{p(x)} = \inf\{\lambda > 0 : Q_{p(x)}(u/\lambda) \leq 1\}.$$

Then the variable exponent Lebesgue and Sobolev spaces are, respectively,

$$L^{p(x)}(\Omega) = \{u : \Omega \to R | ||u||_{p(x)} < \infty\},$$

and

$$W^{1,p(x)}(\Omega) = \{u : \Omega \to R | u \in L^{p(x)}(\Omega), \nabla u \in L^{p(x)}(\Omega)\}.$$

With the norm $||u||_{1,p(x)} = ||u||_{p(x)} + ||\nabla u||_{p(x)}$, $W^{1,p(x)}(\Omega)$ becomes a Banach space.

Definition 2 (Log Holder Continuity): A function $p : \Omega \to R$ is said to be globally log-Holder continuous on Ω if there exists positive constants c_1, c_2, and $a \in R$, such that

$$|p(x) - p(y)| \leq \frac{c_1}{-\log|x-y|}$$
$$|p(x) - a| \leq \frac{c_2}{\log|e+|x||}$$

For all $x \in \Omega$. We denote Log holder continuous function set as $P^{\log}(\Omega)$.

Lemma 1 (Relationship Between Modular and Norm [43]): Let $Q_{p(x)}$ be a modular on X and $u \in X$, then $||u||_{p(x)} \leq Q_{p(x)}(u) + 1$.

Lemma 2 (Embedding Theorem [39]): Let $p(x), q(x) \in P(\Omega)$, and $p(x) \leq q(x)$ for a.e. $x \in \Omega$. Then $L^{q(x)}(\Omega)$ is continuously embedded in $L^{p(x)}(\Omega)$.

Lemma 3 (Convexity [39]): Let $F(\nabla l, x) = |\nabla l|^{p(x)}$, with $p(x) = 1 + \frac{1}{1+w|\nabla c|^2}$ as in Equation (3). Then for each x, $F(\xi, x)$ is convex in ξ.

Lemma 4 (Weak Lower Semi Continuity [39]): Let $F(\xi, x)$ be bounded from below, and the map $\xi \to F(\xi, x)$ be convex in each $x \in \Omega$. Then the energy functional, $I = \int_\Omega F(\nabla l, x)dx$, is weak lower semi-continuous in $W^{1,p(x)}$.

Lemma 5 [43]: Let $p \in P^{\log}(\Omega)$, then for every $u \in W_0^{1,p(\cdot)}(\Omega)$ the inequality

$$||u||_{W^{1,p}(\Omega)} \leq (1 + c\, diam(\Omega))||\nabla u||_{L^{p(x)}(\Omega)}$$

holds.

Lemma 6 [43]: Let Q denote the modular and $u \in X$, then. $||u||_{p(x)} \leq Q(u) + 1$.

Lemma 7 [39]: Let the dimension of Ω be 2, $1 < p(x) \leq 2$. Then $W^{1,p}(\Omega)$ is compactly embedded in $L^{p(x)}(\Omega)$.

Theorem 1: Let $\Omega \subset R^2$ be a bounded set, $u \in L^2(\Omega) \cap BV(\Omega)$, $f \in L^2(\Omega) \cap BV(\Omega)$, $||f||_\infty \leq ||u||_\infty$; $||\nabla f|| < M$ a.e. on Ω. $k \in W^{1,p(x)}(\Omega) \cap L^1(\Omega)$ is equi-continuous and has a compact support D, $k \geq 0$, $\int_\Omega kdx = 1$. Then Equation (3) allows a solution pair $(f_*, k_*) \in (L^2(\Omega) \cap BV(\Omega)) \times (W^{1,p(x)}(\Omega) \cap L^1(\Omega))$.

Proof: There exists a special image-PSF pair (f, k) such that $J < \infty$. Therefore, there must exist a minimizing sequence (f_n, k_n) subject to constraints

$$||k_n(x,y) \otimes f_n(x,y) - u(x,y)||_2^2 \leq M,$$
$$\int |\nabla k_n|^{p(|\nabla c|)} dxdy < M,$$
$$\int |\nabla f_n| dxdy < M,$$

where M denotes a universal positive constant that may differ from line to line. From the Poincare inequality, $\{f_n\}$ is bounded in $L^2(\Omega)$. Then from the Schwartz inequality,

$$||f||_{L^1(\Omega)} \leq ||f||_{L^2(\Omega)} \times \sqrt{|\Omega|}.$$

Hence, $\{f_n\}$ is also bounded in $L^1(\Omega)$. Then from the L^1 precompactness of bounded sets of BV functions on bounded domains and Cantor's diagonal selection method, we can find a subsequence of $\{f_n\}$, for convenience still labeled by $\{f_n\}$, and f_*, such that on any finite disk $B_\rho = \{x \in R^2 : |x| < \rho\}$,

$$f_n \to f_*. \tag{24}$$

With a further round of subsequence selection, we can assume that $f_n \to f_*$ a.e. in R^2.

Since $\int |\nabla k_n|^{p(|\nabla c|)} dxdy < M$, from Lemma 6 $||\nabla k_n||_{L^{p(x)}(\Omega)} < M$, and from Lemma 5, $||k_n||_{W^{1,p}(\Omega)} \leq M$. Thus, since $\int_\Omega |k|dx = 1$, $\{k_n\}$ is bounded in $W^{1,p(x)}(\Omega) \cap L^1(\Omega)$. From Lemma 7 and the L^1 pre-compactness of bounded sets of BV functions on bounded domains, we find a Cauchy subsequence. which we still label as $\{k_n\}$. Similarly, we can find k_* such that on any finite disk $B_\rho = \{x \in R^2 : |x| < \rho\}$,

$$k_n \to k_* \tag{25}$$

With a further round of subsequence selection, we can assume that $k_n \to k_*$ a.e. in R^2.

For any fixed $x \in R^2$, define $k^x(y) = k(x-y)$, $r = R + |x|$ where R is the radius of the support. Then

$$\begin{aligned} k * f(x) &= < k^x(y), f(y) > \\ &= < k^x(y), f(y) >_{B_r} + < k^x(y), f(y) >_{B_r^c} \end{aligned}$$

where $B_r^c = \Omega \backslash B_r$. Hence, restricted on B_r, Equation (24) implies $k_n^x(y) \to k_*^x(y)$ in $L^{p(x)}(B_r)$.

From Lebesgue's dominated convergence theorem, combined with Equation (24) and the boundedness of f_n,

$$< k_*^x, f_n > \to < k_*^x, f_* > . \tag{26}$$

However,

$$|| < k_n^x, f_n >_{B_r} - < k_*^x, f_n >_{B_r} ||_1 \leq M||k_n^x - k_*^x||_1 \to 0. \tag{27}$$

Therefore,

$$< k_n^x, f_n >_{B_r} \to < k_*^x, f_* >_{B_r} . \tag{28}$$

On the complementary $y \in B_r^c$, $|y - x| \geq R$. Thus, $|k_n^x(y)| = |k_n(x-y)| = 0$ in B_r^c. From Lebesgue's dominated convergence theorem,

$$< k_n^x(y), f_n(y) >_{B_r^c} \to < k_*^x(y), f_*(y) >_{B_r^c} . \tag{29}$$

Combined with Equations (28) and (29),

$$k_n * f_n(x) \to k_* * f_*(x), \quad x \in \Omega.$$

Applying Fatou's lemma to the pointwise convergent non-negative sequence,

$$e_n(x) = (k_n * f_n - u(x))^2,$$

then

$$\int_\Omega e_* dxdy \leq \liminf_{n\to\infty} \int_\Omega e_n(x) dxdy. \tag{30}$$

Combined with Lemma 4 and lower semi continuity of TV,

$$\int |\nabla k_*|^{p(|\nabla c|)} dxdy \leq \liminf_{n\to\infty} \int |\nabla k_n|^{p(|\nabla c|)} dxdy,$$
$$\int |\nabla f_*| dxdy \leq \liminf_{n\to\infty} \int |\nabla f_n| dxdy, \tag{31}$$

and with Equations (30) and (31), then

$$J(f_*, k_*) \leq \liminf_{n\to\infty} J(f_n, k_n).$$

From Equations (24) and (25), Fatou's Lemma, and the Poincare inequality,

$$\begin{aligned} ||f_*||_{L^1} &\leq \liminf_{n\to\infty} ||f_n||_{L^1} < \infty \\ ||f_*||_{L^2} &\leq \liminf_{n\to\infty} ||f_n||_{L^2} \leq \liminf_{n\to\infty} |\nabla f| < \infty \\ \int |\nabla f_*| dxdy &\leq \liminf_{n\to\infty} \int |\nabla f_n| dxdy < \infty \\ ||k_*||_{W^{1,p(x)}} &\leq \liminf_{n\to\infty} ||k_n||_{W^{1,p(x)}} < \infty \\ ||k_*||_{L^1} &\leq \liminf_{n\to\infty} ||k_n||_{L^1} < \infty, \end{aligned}$$

So that $f_* \in L^2(\Omega) \cap BV(\Omega)$ and $k_* \in W^{1,p(x)}(\Omega) \cap L^1(\Omega)$.

ACKNOWLEDGMENT
The authors would like to thank the reviewers of this manuscript for their helpful comments and suggestions.

REFERENCES

[1] D. Leger, F. Viallefont, E. Hillairet, and A. Meygret, "In-flight refocusing and MTF assessment of SPOT5 HRG and HRS cameras," *Proc. SPIE*, vol. 4881, pp. 221–331, Apr. 2003.

[2] X. Li *et al.*, "Removing atmospheric MTF and establishing an MTF compensation filter for the HJ-1A CCD camera," *Int. J. Remote Sens.*, vol. 34, no. 4, pp. 1413–1427, 2013.

[3] J. Zhu, W. Hou, X. Zhang, and G. Jin, "Design of a low F-number freeform off-axis three-mirror system with rectangular field-of-view," *J. Opt.*, vol. 17, no. 1, p. 015605, 2015.

[4] W. Hou, J. Zhu, T. Yang, and G. Jin, "Construction method through forward and reverse ray tracing for a design of ultra-wide linear field-of-view off-axis freeform imaging systems," *J. Opt.*, vol. 17, no. 5, p. 055603, 2015.

[5] D. Kundur and D. Hatzinakos, "Blind image deconvolution," *IEEE Signal Process. Mag.*, vol. 13, no. 3, pp. 43–64, May 1996.

[6] P. Campisi and K. Egiazarian, *Blind Image Deconvolution: Theory and Applications*. Boca Raton, FL, USA: CRC Press, 2007.

[7] S. Chaudhuri, R. Velmurugan, and R. Rameshan, *Blind Image Deconvolution: Methods and Convergence*. Cham, Switzerland: Springer, 2014.

[8] M. Cannon, "Blind deconvolution of spatially invariant image blurs with phase," *IEEE Trans. Acoust., Speech, Signal Process.*, vol. ASSP-24, no. 1,pp. 58–63, Feb. 1976.

[9] R. G. Lane and R. H. T. Bates, "Automatic multidimensional deconvolution," *J. Opt. Soc. Amer. A, Opt. Image Sci.*, vol. 4, no. 1, pp. 180–188, 1987.

[10] Y. Senga, K. Minami, S. Kawata, and S. Minami, "Estimation of spectral slit width and blind deconvolution of spectroscopic data by homomorphic filtering," *Appl. Opt.*, vol. 23, no. 10, pp. 1601–1608, 1984.

[11] D. Tzikas, A. Likas, and N. Galatsanos, "Variational Bayesian sparse kernel-based blind image deconvolution with student's-t priors," *IEEE Trans. Image Process.*, vol. 18, no. 4, pp. 753–764, Apr. 2009.

[12] R. Molina, J. Mateos, and A. K. Katsaggelos, "Blind deconvolution using a variational approach to parameter, image, and blur estimation," *IEEE Trans. Image Process.*, vol. 15, no. 12, pp. 3715–3727, Dec. 2006.

[13] C. L. Likas and N. P. Galatsanos, "A variational approach for Bayesian blind image deconvolution," *IEEE Trans. Signal Process.*, vol. 52, no. 8, pp. 2222–2233, Aug. 2004.

[14] D. Kundur and D. Hatzinakos, "A novel blind deconvolution scheme for image restoration using recursive filtering," *IEEE Trans. Signal Process.*, vol. 46, no. 2, pp. 375–390, Feb. 1998.

[15] M. K. Ng, R. J. Plemmons, and S. Qiao, "Regularization of RIF blind image deconvolution," *IEEE Trans. Image Process.*, vol. 9, no. 6, pp. 1130–1134, Jun. 2000.

[16] C. A. Ong and J. A. Chambers, "An enhanced NAS-RIF algorithm for blind image deconvolution," *IEEE Trans. Image Process.*, vol. 8, no. 7, pp. 982–992, Jul. 1999.

[17] T. Kenig, Z. Kam, and A. Feuer, "Blind image deconvolution using machine learning for three-dimensional microscopy," *IEEE Trans. Pattern Anal. Mach. Intell.*, vol. 32, no. 12, pp. 2191–2204, Dec. 2010.

[18] R. Nakagaki and A. K. Katsaggelos, "A VQ-based blind image restoration algorithm," *IEEE Trans. Image Process.*, vol. 12, no. 9, pp. 1044–1053, Sep. 2003.

[19] K. Panchapakesan, D. G. Sheppard, M. W. Marcellin, and B. R. Hunt, "Blur identification from vector quantizer encoder distortion," *IEEE Trans. Image Process.*, vol. 10, no. 3, pp. 465–470, Mar. 2001.

[20] D. Perrone and P. Favaro, "A logarithmic image prior for blind deconvolution," *Int. J. Comput. Vis.*, vol. 117, no. 2, pp. 159–172, 2016.

[21] D. Perrone and P. Favaro, "A clearer picture of total variation blind deconvolution," *IEEE Trans. Pattern Anal. Mach. Intell.*, vol. 38, no. 6, pp. 1041–1055, Jun. 2016.

[22] H. Shen, W. Zhao, Q. Yuan, and L. Zhang, "Blind restoration of remote sensing images by a combination of automatic knife-edge detection and alternating minimization," *Remote Sens.*, vol. 6, no. 8, pp. 7491–7521, 2014.

[23] M. Azadbakht, C. S. Fraser, and K. Khoshelham, "A sparsity-based regularization approach for deconvolution of full-waveform airborne LiDAR data," *Remote Sens.*, vol. 8, no. 8, p. 648, 2016.

[24] T. Choi, "IKONOS satellite on orbit modulation transfer function (MTF) measurement using edge and pulse method," M.S. thesis, Dept. Electr. Eng., South Dakota State Univ., Brookings, SD, USA, 2002.

[25] C. Li and K.-H. Yap, "A soft double regularization approach to parametric blind image deconvolution," *IEEE Trans. Image Process.*, vol. 14, no. 5, pp. 624–633, May 2005.

[26] M. Keuper *et al.*, "Blind deconvolution of widefield fluorescence microscopic data by regularization of the optical transfer function (OTF)," in *Proc. IEEE Conf. Comput. Vis. Pattern Recognit. (CVPR)*, Jun. 2013, pp. 2179–2186.

[27] D. Krishnan, T. Tay, and R. Fergus, "Blind deconvolution using a normalized sparsity measure," in *Proc. IEEE Conf. Comput. Vis. Pattern Recognit. (CVPR)*, Providence, RI, USA, Jun. 2011, pp. 233–240.

[28] Y.-L. You and M. Kaveh, "A regularization approach to joint blur identification and image restoration," *IEEE Trans. Image Process.*, vol. 5, no. 3, pp. 416–427, Mar. 1996.

[29] T. F. Chan and C. K. Wong, "Total variation blind deconvolution," *IEEE Trans. Image Process.*, vol. 7, no. 3, pp. 370–375, Mar. 1998.

[30] L. I. Rudin, S. Osher, and E. Fatemi, "Nonlinear total variation based noise removal algorithms," *Phys. D, Nonlinear Phenomena*, vol. 60, nos. 1–4, pp. 259–268, 1992.

[31] H. Liao and M. K. Ng, "Blind deconvolution using generalized cross-validation approach to regularization parameter estimation," *IEEE Trans. Image Process.*, vol. 20, no. 3, pp. 670–680, Mar. 2011.

[32] H. Shen, L. Du, L. Zhang, and W. Gong, "A blind restoration method for remote sensing images," *IEEE Geosci. Remote Sens. Lett.*, vol. 9, no. 6, pp. 1137–1141, Nov. 2012.

[33] R. L. Lagendijk, J. Biemond, and D. E. Boekee, "Blur identification using the expectation-maximization algorithm," in *Proc. Int. Conf. Acoust., Speech, Signal Process.*, Glasgow, U.K., 1989, pp. 1397–1400.

[34] G. Pavlović and A. M. Tekalp, "Maximum likelihood parametric blur identification based on a continuous spatial domain model," *IEEE Trans. Image Process.*, vol. 1, no. 4, pp. 496–504, Oct. 1992.

[35] S. J. Reeves and R. M. Mersereau, "Blur identification by the method of generalized cross-validation," *IEEE Trans. Image Process.*, vol. 1, no. 3, pp. 301–311, Jul. 1991.

[36] S. D. Babacan, R. Molina, and A. K. Katsaggelos, "Variational Bayesian blind deconvolution using a total variation prior," *IEEE Trans. Image Process.*, vol. 18, no. 1, pp. 12–26, Jan. 2009.

[37] P. Blomgren, T. F. Chan, P. Mulet, and C. K. Wong, "Total variation image restoration: Numerical methods and extensions," in *Proc. IEEE Conf. Image Process.*, Santa Barbara, CA, USA, Oct. 1997, pp. 384–389.

[38] Y. Chen, S. Levine, and M. Rao, "Variable exponent, linear growth functionals in image restoration," *SIAM J. Appl. Math.*, vol. 66, no. 4, pp. 1383–1406, 2006.
[39] F. Li, Z. Li, and L. Pi, "Variable exponent functionals in image restoration," *Appl. Math. Comput.*, vol. 216, no. 3, pp. 870–882, 2010.
[40] Z. Dou, K. Gao, B. Zhang, X. Yu, L. Han, and Z. Zhu, "Realistic image rendition using a variable exponent functional model for retinex," *Sensors*, vol. 16, no. 6, p. 832, 2016.
[41] T. Goldstein and S. Osher, "The split Bregman method for L1-regularized problems," *SIAM J. Imag. Sci.*, vol. 2, no. 2, pp. 323–343, 2009.
[42] H. Cao, X. Liu, S. Li, and X. Zhang, "ZY-3 satellite remote sensing technology," *Spacecr, Rec. Remote Sens.*, vol. 3, pp. 7–16, Sep. 2012.
[43] L. Diening, P. Harjulehto, and P. Hästö, *Lebesgue and Sobolev Spaces With Variable Exponents*. Berlin, Germany: Springer, 2011.
[44] E. Esser, X. Zhang, and T. F. Chan, "A general framework for a class of first order primal-dual algorithms for convex optimization in imaging science," *SIAM J. Imag. Sci.*, vol. 3, no. 4, pp. 1015–1046, 2010.
[45] GF-4 Satellite Introduction. *China Center for Resources Satellite Data and Application Website*. Accessed: Aug. 3, 2017. [Online]. Available: http://www.cresda.com/EN/satellite/9907.shtml
[46] D. Krishnan and R. Fergus, "Fast image deconvolution using hyper-Laplacian priors," in *Proc. Adv. Neural Inf. Proces. Syst. (NIPS)*, Vancouver, B.C., Canada. Dec 2009, pp. 1033–1041.

KUN GAO received the B.A. degree in electrical engineering and the Ph.D. degree in instrument science and engineering from Zhejiang University, China, in 1995 and 2002, respectively. From 2002 to 2004, he was a Post-Doctoral Fellow with Tsinghua University, China. Since 2005, he has been with the Beijing Institute of Technology, China, with a focus on infrared technology and real-time image processing. He is a member of the Optical Society of China.

ZHENYU ZHU received the B.E. degree in optical information science and technology from the North University of China in 2011. He is currently pursuing the Ph.D. degree with the Beijing Institute of Technology. His research interests include image processing and image super-resolution.

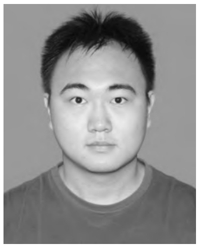

ZEYANG DOU received the B.E. degree in mathematics from Baoding University, China, in 2012, and the M.S. degree in computational mathematics from the Communication University of China, China, in 2016. He is currently pursuing the Ph.D. degree with the Beijing Institute of Technology. His research interests include image processing, machine learning, and deep learning.

LU HAN received the B.E. degree in electronic engineering from the North University of China in 2013, and the M.S. degree in optical engineering from the Beijing Institute of Technology in 2015, where she is currently pursuing the Ph.D. degree. Her research interests include image processing and ground calibration.